Paulo David Rodrigues Santos

Modelação ab-initio de defeitos de radiação em células solares de Si.

Ab-initio modeling of radiation defects in Si solar cells.

Paulo David Rodrigues Santos

Modelação ab-initio de defeitos de radiação em células solares de Si.

Ab-initio modeling of radiation defects in Si solar cells.

Dissertação apresentada à Universidade de Aveiro para cumprimento dos requisitos necessários à obtenção do grau de mestre em Física, realizada sob orientação científica de Dr. J. Coutinho, do departamento de Física da Universidade de Aveiro

Dissertation presented at the University of Aveiro for the fulfilling of the requirements for obtaining the master's degree in Physics, supervised by Dr. J. Coutinho, from the Department of Physics of the University of Aveiro

o júri / the jury

presidente / president

Professor Doutor Manuel António dos Santos Barroso
Professor Auxiliar da Universidade de Aveiro.

vogais / examiners committee

Doutor Apostolos Marinopoulos
Investigador Auxiliar, faculdade de Ciências e Tecnologia, Universidade de Coimbra.

Doutor José Pedro de Abreu Coutinho
Investigador auxiliar da Universidade de Aveiro.

agradecimentos / acknowledgements

First of all, I would like to thank my supervisor José Coutinho, for his constant avaiability and helpful advice during the whole process that led to the completion of this document.
I also thank everyone who had a decisive contribution in some particular stages of this task. In special, Alexandra Carvalho, who gave important input to the scientific argumentation and results presented in this thesis, particularly in its last chapter, and Daniel Gouveia, with his help with many grammar-related questions and LateX troubleshooting.
Finally I would like to thank the support from Fundação para a Ciência e a Tecnologia (FCT) under the contract PEST-C/CTM/LA0025/2011.

Palavras chave Silício, defeitos, degradação, células solares, lacunas

Resumo

Neste trabalho são estudados defeitos que são provocados por radiação e que causam a degradação do funcionamento de dispositivos tais como células solares ou detectores. São abordados, em particular, os problemas da formação de multilacunas em detectores de radiação e da degradação da eficiência de células solares baseadas em silício dopado com Boro quando expostas à luz.

O documento divide-se em quatro capítulos. No primeiro capítulo é descrita a teoria do funcional da densidade que serve de base para os nossos cálculos. Os métodos e aproximações utilizados são apresentados. No capítulo dois é discutido o problema da formação de agregados de multilacunas em detectores de radiação baseados em silício. A estabilidade e actividade eléctrica destes defeitos são avaliadas. Contrariamente às anteriores previsões, observamos a existência de estados localizados no gap produzidos por estas estruturas, nas suas configurações mais estáveis. Os níveis elétricos associados que foram obtidos explicam alguns dos resultados experimentais presentes na literatura. Nos capítulos três e quatro são abordados dois modelos candidatos para a explicação do problema da degradação da eficência de células solares baseadas em silício produzido pelo método de Czochralski dopado com Boro. No capítulo três o modelo baseado no defeito B_sO_{2i} é discutido. Este modelo pressupõe a existência de um comportamento bi-estável do dímero de oxigénio, (O_{2i}), que está dependente da localização do nível de Fermi no gap. Esta bi-estabilidade permite a difusão do O_{2i} no cristal, podendo ser capturado por átomos de Boro em posições substitucionais formando o defeito B_sO_{2i} responsável pela degradação. Os cálculos apresentados neste trabalho confirmam a existência de duas estruturas estáveis do O_{2i}, para os estados de carga neutro e duplo positivo. Contudo, apenas foi encontrada correspondência entre os modos de vibração locais do defeito e o espectro de absorção no infravermelho para a estrutura no estado de carga neutro, dificultando a validação do modelo. No capítulo quatro é apresentado o modelo baseado no defeito B_iO_{2i}. Este último pressupõe a formação de defeitos de boro intersticial no curso do arrefecimento do cristal, que podem difundir no cristal e ser capturados por dímeros de oxigénio, formando o B_iO_{2i}. Contudo os nossos cálculos relativos à energia de formação de defeitos de boro intersticional demonstram que a formação destes defeitos nas condições supracitadas é muito improvável, excluindo este modelo.

Keywords Silicon, defects, degradation, solar cells, vacancies

Abstract

In this work, radiation induced defects responsible for operational degradation of devices such as solar cells or detectors are studied. In particular, problems related to the formation of multivacancies in radiation detectors and light-induced efficiency degradation in boron-doped silicon solar cells are addressed.

The document is divided in four chapters. In the first one, the Density Functional Theory, which is the framework for our calculations, is described. The methods and approximations used are presented. In chapter two, the problem of the formation of multivacancy clusters in silicon-based detectors is discussed. The stability and electrical activity of these defects are scrutinized. Contrary to previous predictions, we observe the existence of localized states in the gap produced by these structures, in their most stable configurations. The associated electrical levels that were obtained explain some of the experimental data reported in the literature. In chapters three and four, two candidate models for the explanation of the light-induced efficiency degradation in Boron-doped Czrochralski-grown silicon solar cells are covered. In chapter three the model based in the B_sO_{2i} defect is discussed. This model assumes the existence of a bi-stable behavior of the oxygen dimmer, (O_{2i}), depending on the position of the Fermi level in the gap. This bi-stability allows the diffusion of the O_{2i} in the crystal, which may lead to its capture by Boron atomos in substitutional positions, leading to the formation of the B_sO_{2i} defect, responsible for the degradation. The calculation presented in this work confirm the existence of two different stable structures for the O_{2i}, for the neutral and double positively charged states. However, a match between the local vibrational modes of the defect and the infrared absortion spectra was found only for the neutral charge state configuration, hindering the validation of this model. Chapter four presents a model based on the B_sO_{2i} defect. This one assumes the formation of interstitial boron defects in the course of crystal cooling, which may diffuse across the crystal and be trapped by oxygen dimmers. However, our calculations concerning the formation energy of interstitial boron defects show that the formation of these defects in the aforementioned conditions is very unlikely, which rules out this model.

Contents

List of Figures

List of Tables

Chapter 1

Theoretical framework

1.1 The many-body problem

The calculation of physical observables in large molecules or solids implies solving the Schrödinger equation for a large set of atomic particles, i.e., electrons and nucleons. Considering the entire atomic nucleus as a single particle, in a stationary and non-relativistic problem, the Schrödinger equation for a set of N_{e} electrons and N_{n} atomic nuclei in the absence of a external field is:

$$\hat{H}\Psi = E\Psi, \tag{1.1}$$

where $\hat{H}$ is the Hamiltonian operator for this system, which, in atomic units, can be written as:

$$\begin{aligned}
\hat{H} &= \hat{T}_{\mathrm{e}} + \hat{T}_{\mathrm{n}} + \hat{V}_{\mathrm{e-e}} + \hat{V}_{\mathrm{n-n}} + \hat{V}_{\mathrm{n-e}} = \\
&= -\frac{1}{2}\sum_{i}^{N_{\mathrm{e}}} \nabla_i^2 - \sum_{\alpha}^{N_{\mathrm{n}}} \frac{1}{2M_\alpha}\nabla_\alpha^2 + \\
&\quad + \frac{1}{2}\sum_{i,j=1;i\neq j}^{N_{\mathrm{e}}} \frac{1}{\mid \mathbf{r}_i - \mathbf{r}_j \mid} + \frac{1}{2}\sum_{\alpha,\beta=1;\alpha\neq\beta}^{N_{\mathrm{n}}} \frac{Z_\alpha Z_\beta}{\mid \mathbf{R}_\alpha - \mathbf{R}_\beta \mid} - \\
&\quad - \sum_{i,\alpha=1}^{N_{\mathrm{e}},N_{\mathrm{n}}} \frac{Z_\alpha}{\mid \mathbf{r}_i - \mathbf{R}_\alpha \mid},
\end{aligned} \tag{1.2}$$

where $\hat{T}$ and $\hat{V}$ stand for kinetic energy and Coulumbic interaction terms respectively. $\mathbf{R}_\alpha$,M_α and Z_α, are the position, mass and charge of the α -th atomic nucleus, and r_i is the position of the i -th electron. Subscripts n and e stand for nuclei and electron related terms respectively. For this Hamiltonian, the total wave function Ψ of the system will be a function of the N_{n} nuclei coordinates and of the N_{e} sets of spatial coordinates and spin quantum numbers on which the electron wave functions are dependent.

$$\Psi = \Psi(\mathbf{R}_1, \ldots, \mathbf{R}_{N_n}, \mathbf{r}_1, s_1, \ldots, \mathbf{r}_{N_e}, s_{N_e}). \tag{1.3}$$

The analytical solution for Eq. 1.2 is only known for simple problems like the hydrogen atom and the He^+ ion (Schiff, 1968). Given the fact that Ψ depends on $3N_\mathrm{n} + 4\sum_\alpha Z_\alpha$ scalar variables, the computational treatment of this equation for problems with technological relevance becomes impracticable. Consequently, some approximations must be made in order to simplify the problem.

1.2 The Born-Oppenheimer approximation

Since the electron mass is 2000 times lower than the mass of a neutron or a proton, it is assumed that the electrons respond adiabatically to the nuclear motion (Born and Oppenheimer, 1925). Thus, in the electron point of view, the atomic nuclei can be considered as virtually static. Based on this assumption, Born and Oppenheimer proposed that the total wave function Ψ can be approximated to a product of two wave functions $\psi_\mathbf{R}(\mathbf{r})$ and $\chi(\mathbf{R})$, where $\psi_\mathbf{R}(\mathbf{r})$ is a function all of the electrons' coordinates and $\chi(\mathbf{R})$ is a function of all nuclear coordinates, i.e.:

$$\Psi(\mathbf{r},\mathbf{R}) = \psi_\mathbf{R}(\mathbf{r})\chi(\mathbf{R}), \tag{1.4}$$

where $\mathbf{r}$ and $\mathbf{R}$ represent the set of all spatial and spin coordinates of the electrons and nuclei, respectively. It shall be noted that the electron part of the wave function $\psi_\mathbf{R}(\mathbf{r})$ still depends on the nuclear coordinates in a parametric way. By performing this substitution, Equation 1.1 can be re-writen:

$$\begin{aligned}\hat{H}\psi_\mathbf{R}(\mathbf{r})\chi(\mathbf{R}) &= (E_\mathrm{e} + E_\mathrm{n})\psi_\mathbf{R}(\mathbf{r})\chi(\mathbf{R}) \\ -\sum_\alpha^{N_n} \frac{1}{2M_\alpha}&[\chi(\mathbf{R})\nabla_\alpha^2\psi_\mathbf{R}(\mathbf{r}) + 2\nabla_\alpha\psi_\mathbf{R}(\mathbf{r}).\nabla_\alpha\chi(\mathbf{R})],\end{aligned} \tag{1.5}$$

where E_e and E_n represent eigenvalues of the following differential equations:

$$(\hat{T}_\mathrm{n} + \hat{V}_{\mathrm{n-n}})\chi = E_\mathrm{n}\chi, \tag{1.6}$$

$$(\hat{T}_\mathrm{e} + \hat{V}_{\mathrm{e-e}} + \hat{V}_{\mathrm{e-n}})\chi = E_\mathrm{e}\chi. \tag{1.7}$$

Since, in atomic units, $M_\alpha \approx 4000Z_\alpha$, the last term of 1.5 can be negleted and our many-body problem can be now described by the Equations 1.6 and 1.7. We are now looking for the set of nuclear coordinates that minimize the eigenvalues $E_\mathrm{e}(\mathbf{R})$ which are obtained from the only-electron Shrödinger Equation 1.7.

1.3 The variational method

For Hamiltonians such as described in Eq. 1.2, the ground state can be approximately obtained with the application of the variational principle. The varionational principle states that the mean value of a given Hamiltonian $\hat{H}$ in the state $\mid \Psi\rangle$ is given by

$$\langle\hat{H}\rangle = \frac{\langle\Psi \mid \hat{H} \mid \Psi\rangle}{\langle\Psi \mid \Psi\rangle}, \tag{1.8}$$

and is stationary in the vicinity of the discrete eigenvalues of $\hat{H}$. In other words, the eigenvalues of $\hat{H}$ are local minima of $\langle \hat{H} \rangle$ with respect to $\mid \Psi \rangle$.
This variational principle has two direct consequences:

1. For any trial state $\mid \Psi \rangle$:

$$\langle \hat{H} \rangle \geq E_0, \tag{1.9}$$

   where E_0 is the lowest eigenvalue of the Hamiltonian $\hat{H}$.

2. Full minimization of $\langle \hat{H} \rangle$ with respect to all degrees of freedom in Ψ will give the true ground state Ψ_0 and groud state energy E_0, i.e.:

$$E_0 = \min_{\Psi} E[\Psi]. \tag{1.10}$$

1.4 Density Functional Theory

1.4.1 Introduction

In 1964, Hohemberg and Kohn proposed and demonstrated two theorems, which mathematically support that the total ground state energy $E[n(\mathbf{r})]$, for a known many-electron Hamiltonian, can be described, without any approximation, in terms of the electron charge density $n(\mathbf{r})$ at the ground state of the system $\mid \Psi_0 \rangle$, which is given by:

$$n(\mathbf{r}) = \langle \Psi_0 \mid \Psi_0 \rangle. \tag{1.11}$$

Those two theorems form the basis for the Density Functional Theory (DFT), which is used in most of today's state-of-the-art electronic structure calculations, including the ones performed in this work. In this section we present the two Hohemberg-Kohn theorems and the Kohn-Sham equations from them derived. Approximations for the electron exchange and correlation potentials are also presented.

1.4.2 Hohenberg-Kohn theorems

For a normalized and non-degenerate ground state $\mid \Psi_0 \rangle$ in the absence of a magnectic field:

1. **Hohenberg-Kohn first theorem:** *The external potential is determined, within a trivial additive constant, by the electron density $n(\boldsymbol{r})$.*

   Let us again consider the many-electron Hamiltonian, where the electrons are subject to an external electron potential $v_{\text{ext}}(\mathbf{r})$.

$$\hat{H} = \hat{T}_{\text{e}} + \hat{V}_{\text{e-e}} + \hat{V}_{\text{ext}}, \tag{1.12}$$

where $\hat{T}_{\rm e}$ is the electron kinetic energy operator,$\hat{V}_{\rm e-e}$ is the operator for the electron-electron interactions and $\hat{V}_{\rm ext}$ is such that:

$$\hat{V}_{\rm ext} \mid \Psi_0\rangle = \mid v_{\rm ext}\Psi_0\rangle, \tag{1.13}$$

where $v_{\rm ext}$ stands for all the potentials that are external to the electrons. One can show that the relation presented in Eq. 1.11 can be reversed, which, in other words, means that the ground state of a given system $\mid \Psi_0\rangle$ is always a unique functional of $n(\mathbf{r})$. Thus, the expected value for the ground state of any observable O is also a unique functional of $n(\mathbf{r})$:

$$O = \langle \Psi_0[n(\mathbf{r})] \mid \hat{O} \mid \Psi_0[n(\mathbf{r})]\rangle. \tag{1.14}$$

Given this, we can define the functional $F[n(\mathbf{r})]$ as:

$$F[n(\mathbf{r})] = \langle \Psi[n(\mathbf{r})] \mid \hat{T}_{\rm e} + \hat{V}_{\rm e-e} \mid \Psi[n(\mathbf{r})]\rangle. \tag{1.15}$$

Since $F[n(\mathbf{r})]$ is only electron dependent, it will remain the same, regardless of the external potentials that are applied. Therefore it can be regarded as an universal (system-independent) value.

On the other hand it can be also shown that $v_{\rm ext}$ is also a unique functional of $n(\mathbf{r})$, and the expected value of $\hat{V}_{\rm ext}$ will become:

$$\begin{aligned} V_{\rm ext}[n(\mathbf{r})] &= \langle \Psi[n(\mathbf{r})] \mid \hat{V} \mid \Psi[n(\mathbf{r})]\rangle \\ &= \int v_{\rm ext} n(\mathbf{r}) d\mathbf{r}. \end{aligned} \tag{1.16}$$

From Eqs. 1.15 and 1.16, the following expression for the total ground state energy can be obtained:

$$E[n(\mathbf{r})] = F[n(\mathbf{r})] + \int v_{\rm ext} n(\mathbf{r}) d\mathbf{r}, \tag{1.17}$$

which summarizes the first Hohenberg-Kohn theorem.

2. **Hohenberg-Kohn second theorem:** *For a trial density* $\tilde{n}(\boldsymbol{r})$*, such that* $\tilde{n}(\boldsymbol{r}) \geq 0$ *and* $\int \tilde{n}(\boldsymbol{r}) d\boldsymbol{r} = N$:

$$E_0 \leq E[\tilde{n}(\mathbf{r})]. \tag{1.18}$$

This is basically the application of the variational principle. Hence, by performing a full minimization of $E[n(\mathbf{r})]$ with respect to $n(\mathbf{r})$, we can obtain the exact value for the ground state energy E_0 and the exact form of the ground state total charge density n_0 and wave-function Ψ_0 as well.

1.4.3 Kohn-Sham equations (Kohn and Sham, 1965)

Due to the terms that describe the interactions between electrons, the exact form of $F[n(\mathbf{r})]$ cannot be determined. However, for systems where the charge density has no abrupt variations, the solutions for the total energy and charge density can be obtained by approximation under the application of the DFT principles. With that aim, let us consider an auxiliary system with N electrons with no interactions between them. We can pick an external applied potential v_{s} such that the charge density $n(\mathbf{r})$ will be exactly the same as it would be for the equivalent interacting system. For a non interacting system, the charge density $n(\mathbf{r})$ is given by:

$$n(\mathbf{r}) = \sum_{l}^{N} \mid \psi_l(\mathbf{r}) \mid^2, \tag{1.19}$$

and the correspondent set of Schröedinger equations becomes:

$$-\frac{1}{2}\nabla^2\psi_l + v_{\mathrm{s}}\psi_l = \epsilon_l\psi_l, \tag{1.20}$$

where ψ_l is a non interacting electron orbital and ϵ_l is the corresponding eigenvalue. These orbitals are called *Kohn-Sham Orbitals*. We must bear in mind that they have no true physical meaning, since they only describe this auxiliary non-interacting system. The total energy functional for the equivalent interacting system, within the DFT formalism, is given by (Parr and Yang, 1989):

$$E_{\mathrm{tot}}[n(\mathbf{r})] = T[n(\mathbf{r})] + \int n(\mathbf{r})v(\mathbf{r})d\mathbf{r} + \int \frac{n(\mathbf{r})n(\mathbf{r}')}{\mid \mathbf{r} - \mathbf{r}' \mid} d\mathbf{r}d\mathbf{r}' + E_{\mathrm{xc}}, \tag{1.21}$$

where $T[n(\mathbf{r})]$ is the expected value for the total kinectic energy of the non interacting system, i.e.:

$$T[n(\mathbf{r})] = \sum_{l}^{N} \langle \psi_l \mid -\frac{1}{2}\nabla^2 \mid \psi_l \rangle. \tag{1.22}$$

The E_{xc} term includes the exchange and correlation potential energies and its exact form is unknown. Standard approximations for E_{xc} are discussed later on. From Eq. 1.21 we can extract the from of the auxiliary potential v_{s}:

$$v_{\mathrm{s}} = v(\mathbf{r}) + \int \frac{n(\mathbf{r'})}{\mid \mathbf{r} - \mathbf{r'} \mid} d\mathbf{r'} + \frac{\delta E_{\mathrm{xc}}}{\delta n(\mathbf{r})}, \tag{1.23}$$

which can be replaced on Eq.1.20.
Equations 1.19 and 1.20 form a set of $N+1$ equations that can be solved in a self-consistency cycle: we start with a trial charge density $\tilde{n}(\mathbf{r})$ and replace the potential v_{s} in 1.20, which can be solved in order to obtain a set of eigenfunctions ψ_l and eigenvalues ϵ_l. From those eigenfunctions, and by using Eq. 1.19, a new charge density can be computed. This 2-step process is repeated until the charge density does not change significantly between cycles. Once the final values of $n(\mathbf{r})$ and ψ_l are obtained, we can replace them in Eq. 1.21 and determine the total energy of the many electron system.

1.4.4 The exchange and correlation functional

As it was said in the previous section, the exact form of the exchange-correlation functional E_{XC} cannot be determined for the majority of heterogeneous systems. However, some approximations can be made. One of the important properties of this functional is that it is non-local, because it depends not only on the charge density $n(\mathbf{r})$ on a given point $\mathbf{r}_i$, but also on all its spatial derivatives, i.e.:

$$E_{\mathrm{xc}} = E_{\mathrm{xc}}[n(\mathbf{r}), \boldsymbol{\nabla} n(\mathbf{r}) \boldsymbol{\nabla}(\boldsymbol{\nabla} n(\mathbf{r}))...]. \tag{1.24}$$

The most straightforward approximation is to assume that E_{xc} depends only on the local charge density, that is, a local behaviour of E_{xc} is assumed. This approximation is called LDA (local density approximation) or LSDA (local spin density approximation) for non-zero spin systems (Kohn and Sham, 1965; von Barth and Hedin, 1972; Perdew and Zunger, 1981). In the LSDA approach the local charge density is separated in spin-up $n_\uparrow$ and spin-down $n_\downarrow$ densities. In both approximations, the exchange correlation energy is usually separated in two terms corresponding to the exchange $E_{\mathrm{x}}[n]$ and correlation $E_{\mathrm{c}}[n]$ parts.

The exchange part can be obtained analytically from the Hartree-Fock method, and in the LSDA notation becomes:

$$E_{\mathrm{x}}[n] = -\frac{3}{2}\left(\frac{3}{4\pi}\right)^{\frac{1}{3}}\left(n_\uparrow^{\frac{4}{3}} + n_\downarrow^{\frac{4}{3}}\right). \tag{1.25}$$

The correlation part is more complicated, and several approximation techniques are applied. For systems within a high density regime, perturbation theory is applied. For low density regimes, a Green function quantum Monte Carlo method is applied (Ceperley, 1978; Ceperley and Alder, 1980), and a parameterized functional is fitted to its numerical results. There are several parameterizations available, such as the VWN parameterization (Vosko *et al*, 1908) or the PW (Pardew and Wang, 1992). Another common approximation consists in a first-order expansion of E_{XC} in n and $\boldsymbol{\nabla} n$ dependent terms, and it is called GGA (generalized gradient approximation) (Perdew, 1991).

1.5 Pseudopotentials

The Pseudopotential method is a way to describe the screened nuclei seen by valence electrons which is caused by the electrons in the core states. This approach allows us to remove terms regarding core-electron states from the many-body Hamiltonian and replace them with a pseudopotential, leaving only the valence-electron eigen states and respective energies to be determined. By doing so, the following issues can be overcome:

- **The distinct behaviour of core states and valence states**
  Core electrons are strongly coupled to the nuclei by a coulombic potential, and, due to their high kinetic energy, their wavefunctions present strong oscillations. In addition, the valence electrons are weakly coupled to atomic nuclei and their wave functions will follow the molecular or lattice symmetry, with soft variations. Given the diverse nature of core-electron and valence-electron wave functions, the number of basis functions required to fit all of these wave functions would become prohibitively large.

- **The lack of precision in total energies**
  The inclusion of the core electrons in the calculations would result in huge total energies. As we are only interested in energy differences between similar systems, this would lead to a big loss in the accuracy of the final result.

However, this method comes with the cost of two approximations:

1. the *frozen core approximation*
   This approximation assumes that core electron wave functions remain unperturbed when the atom is transferred to different specific environments

2. the *small core approximation*
   It is assumed that the overlap between core-electron and valence-electron wave functions is negligible. For this reason we can neglect exchange-correlation matrix elements that link core-electron and valence-electron states, allowing us to treat exchange correlation terms regarding core and valence electrons separately: $E_{\rm xc}(n_{\rm core} + n_{\rm valence}) \approx E_{\rm xc}(n_{\rm core}) + E_{\rm xc}(n_{\rm core})$

Detailed information on the pseudopotential method and frozen and small core approximations has been extensively reported (Harrison, 1966; Brust, 1968; Stoneham, 1975; Heine, 1970; Pickett, 1989).

Basic formulation and Transferibility

A pseudopotential is transferable if it can reproduce the properties of valence electrons in several different environments. The construction of a pseudopotential is made by removing the valence electrons, leaving behind an *ionic-pseudoptotential*. Within the density functional framework it comes:

$$\hat{V}^{\rm ps}_{\rm ion}(\mathbf{r}) = \hat{V}^{\rm ps}(\mathbf{r}) - \int \frac{n^{\rm ps}(\mathbf{r})}{\mid \mathbf{r} - \mathbf{r'} \mid} d\mathbf{r'} - \hat{V}_{\rm xc}[n(\mathbf{r})], \tag{1.26}$$

where $V^{\rm ps}_{\rm ion}(\mathbf{r})$ is the pseudopotential of the neutral atom and $n^{\rm ps}(\mathbf{r})$ is the charge-density from the valence states, and it is given by:

$$n^{\rm ps}(\mathbf{r}) = \sum_{\lambda} \mid \psi^{\rm ps}_{\lambda}(\mathbf{r}) \mid^2 . \tag{1.27}$$

All the calculations presented in this work use the Hartwigsen-Goedecker-Hutter (HGH) pseudopotentials (Hartwigsen *et al*, 1998), which are a relativistic generalization of separable dual-space Gaussian pseudopotentials. These pseudo-potentials have the particular feature of including relativistc efects that occur in heavy elements of the periodic table on their formulation. The extensive list of the HGH pseudo potentials can be consulted in the referred publication.

1.6 The AIMPRO code

1.6.1 Periodic systems

From the Bloch theorem we know that, for periodic atomic systems like crystals, the charge density assumes the periodicity of the system in the real-space. In those cases, the

calculation of observables which are functionals of $n(\mathbf{r})$ becomes easier when performed in the reciprocal space. With that aim, the charge density is expanded in a planewave basis with the aid of a Fourier transform. All the integrations in the reciprocal space are made over the Brillouin zone.

The suppercell approximation

Let us consider a perfect crystaline material represented by a unit cell with volume v_0 defined by unit vectors $\mathbf{a}_i$, with $i = 1, 2, 3$, and containing n_a atoms with spatial coordinates $\mathbf{r}_j$, with $j = 1, 2, ..., n_a$ with respect to the origin of the unit cell. The Bravais lattice points $\mathbf{l_n}$ are defined as:

$$\mathbf{l_n} = \sum_i n_i \mathbf{a}_i, \tag{1.28}$$

and the reciprocal latice unit vectors are defined as:

$$\mathbf{G}_i = 2\pi \frac{\mathbf{a}_j \times \mathbf{a}_k}{\mathbf{a}_i.(\mathbf{a}_j \times \mathbf{a}_k)}, \tag{1.29}$$

where i, j, k cyclically permute between the values of $1, 2$ and 3. A supercell with volume ω can be defined by the linear transformation W that operates on the unit vectors $\mathbf{a}_i$:

$$\mathbf{A}_j = \sum_{i=1}^{3} W_{ij} \mathbf{a}_i, \tag{1.30}$$

where W_{ij} are integer matrix elements, and $\mathbf{A}_j$ are the unit vectors of the supercell with the respective lattice defined by $\mathbf{L_n} = \sum_i n_i \mathbf{A}_i$, where n_i can be any integer.

The ratios between number of atoms and volumes of the original unit cell and the supercell are both given by $\det(W)$, and so we can write:

$$\begin{aligned} \omega &= \det(W) v_0 \\ N_a &= \det(W) n_a, \end{aligned} \tag{1.31}$$

where N_a is the number of atoms of the supercell, whose locations $\mathbf{R}_i$, with $i = 1, .., N_a$ relatively to the supercell origin can be obtained from the following relation:

$$\mathbf{R}_i = \mathbf{l_n} + \mathbf{r}_k, \text{ for all } \mathbf{R}_i - \mathbf{R}_j \neq L_m, \tag{1.32}$$

where k can take any value in the range $1 \leq k \leq n_a$ and n can be any integer. The second condition implies that both atomic positions $\mathbf{R}_i$ and $\mathbf{R}_j$ can never differ by a super lattice vector $\mathbf{L}_m$, ensuring that the respective atoms are included in the same supercell.

The corresponding cell in the reciprocal space, defined by the unit vectors $\mathbf{g}_j$, will have a volume $\det(W)$ times smaller than the one defined by the $\mathbf{G}_j$ vectors. The equivalent linear transformation for the reciprocal space will be given by:

$$\mathbf{g}_j = \sum_{i=1}^{3} L_{ij}^{-1} \mathbf{G}_i, \tag{1.33}$$

where L_{ij}^{-1} are matrix elements of the linear operator L^{-1}. The supercell method is applied within the AIMPRO code in order to model localized provlems in solids, surfaces and nanostructures.
The characterization of point defects in a crystalline bulk environment with the application of this method requires special care in the choice of the size and shape of the supercell. Let us consider a point defect included in a crystalline supercell. Since the supercell is repeated through space due to periodic boundary conditions, any defect that is included in it will also be repeated. Hence, several images of the defect are generated along the latice (regardless of its position in the supercell). If the size or shape of the supercell are not correctly chosen, there might be interactions of many kinds between the considered defect and its images, like coulombic, elastic, dipolar or quadrupolar interactions.

Real space basis functions

Unlike many supercell calculations that use plane-wave basis functions to expand the Kohn-Sham orbitals in the real space, the AIMPRO code makes use of a set of Bloch wave functions $\mathrm{B}_{\mathbf{k}i}(\mathbf{r})$. Those Bloch wave functions are built in the following way:

$$\mathrm{B}_{\mathbf{k}i}(\mathbf{r}) = \frac{1}{\sqrt{N_L}} \sum_{n=1}^{N_L} \Phi_i(\mathbf{r} - \mathbf{L_n}) e^{\mathbf{i}\mathbf{k}.\mathbf{L_n}}. \tag{1.34}$$

This sum is made over N_L lattice vectors L_n. Φ_i are Cartesian-Gaussian orbital functions centered at $\mathbf{R}_i$ and are defined as:

$$\Phi_i(\mathbf{r}) = (x - R_{ix})^{l_1}(y - R_{iy})^{l_2}(z - R_{iz})^{l_3} e^{-a_i(\mathbf{r}-\mathbf{R}_i)^2}, \tag{1.35}$$

where l_1, l_2 and l_3 are integers. Φ_i describes a s, p or d orbital if $\sum_{i=1}^{3} l_i$ assumes the value of 0, 1 or 2 respectively. So, the expansion of the Kohn-Sham orbitals in terms of this Bloch-function basis is written as:

$$\Psi_{\mathbf{k}\lambda}(\mathbf{r}) = \sum_j c_{\mathbf{k}\lambda,i} \mathrm{B}_{\mathbf{k}i}(\mathbf{r}), \tag{1.36}$$

where $c_{\mathbf{k}\lambda,i}$ are the coefficients of the expansion. The charge density can be easily determined from the Kohn-Sham orbitals, and comes as:

$$\begin{aligned} n(\mathbf{r}) &= \sum_{i,j,\mathbf{k}} b_{ij}(\mathbf{k}) B^*_{\mathbf{k}i}(\mathbf{r}) \mathrm{B}_{\mathbf{k}j}(\mathbf{r}) \\ b_{ij}(\mathbf{k}) &= \sum_{\lambda} f_{\mathbf{k}\lambda} c^*_{\mathbf{k}\lambda,i} c_{\mathbf{k}\lambda,j}, \end{aligned} \tag{1.37}$$

where $f_{\mathbf{k}\lambda}$ gives the ocupancy of the $\mathbf{k}\lambda$ state, taking the value of 2 for fully occupied states and 0 for the empty ones.

Reciprocal space basis functions

In a system with periodic boundary conditions, there are several quantities that are easier to evaluate in the reciprocal space. That is the case of the Hartree and exchange correlation

energies. For a given **k** point, the Kohn-Sham orbitals are expanded in an orthogonal basis, accordingly to the following equation:

$$\psi_{\mathbf{k}\lambda} = \sum_{\mathbf{G}} c_\lambda(\mathbf{G}) e^{i(\mathbf{k}+\mathbf{G}).\mathbf{r}}, \tag{1.38}$$

where **G** are vectors that form a discrete vector grid, limited within a sphere with radius defined G_{cut}, hence limiting the size of the expansion basis, and, consequently, its level of accuracy. In practice, G_{cut} is defined by an energy cut-off value E_{cut} defined as:

$$E_{\text{cut}} = \frac{1}{2} G_{\text{cut}}^2. \tag{1.39}$$

Brillouin Zone integration

As it was mentioned before, many of the integrals in DFT for periodic systems are performed in the reciprocal space over the Brillouin Zone. Usually, the functions to be integrated have no simple analytic form and require a numeric integration within a dense grid of points in k-space, and therefore at large computational cost. To avoid this, several approximations were proposed. The AIMPRO code applies the Brillouin-Zone sampling method proposed by Monkhorst and Pack (Monkhorst and Pack, 1976; Pack and Monkhorst, 1977). The method consists in approximating the average of the integrand function $f(\mathbf{k})$ in the following way:

$$\tilde{f} = \frac{\Omega}{2\pi^3} \int f(\mathbf{k}) d\mathbf{k} \approx \frac{1}{N} \sum_i^N f(\mathbf{k}_i). \tag{1.40}$$

Instead of a full integration over the Brillouin zone, a sum over special **k**-points $\mathbf{k}_i$ is applied.

1.6.2 Calculation of observables

Structure Optimization

As mentioned above, once the Kohn-Sham equations are solved, we are able to determine the total density $n(\mathbf{r})$ and energy E_{TOT} of a system with fixed atomic positions. However, for most of the situations we are interested in, the equilibrium atomic positions of the system are unknown. The equilibrium configurations of the system correspond to local minima of the total energy with respect to all atomic coordinates. The search for these local minima follows an algorithm based on a conjugated gradient minimization method.
The process consists on the determination of the forces acting on each atom $\mathbf{F}_\alpha$, which can be obtained from the gradient of the total energy of the system with respect to the spacial coordinates of each atom $-\boldsymbol{\nabla}_\alpha E_{\text{TOT}}$, i.e.:

$$\mathbf{F}_\alpha = -\boldsymbol{\nabla}_\alpha E_{\text{TOT}}. \tag{1.41}$$

Those derivatives can be evaluated with the application of the Hellman-Feynman theorem (Epstein *et al*, 1967):

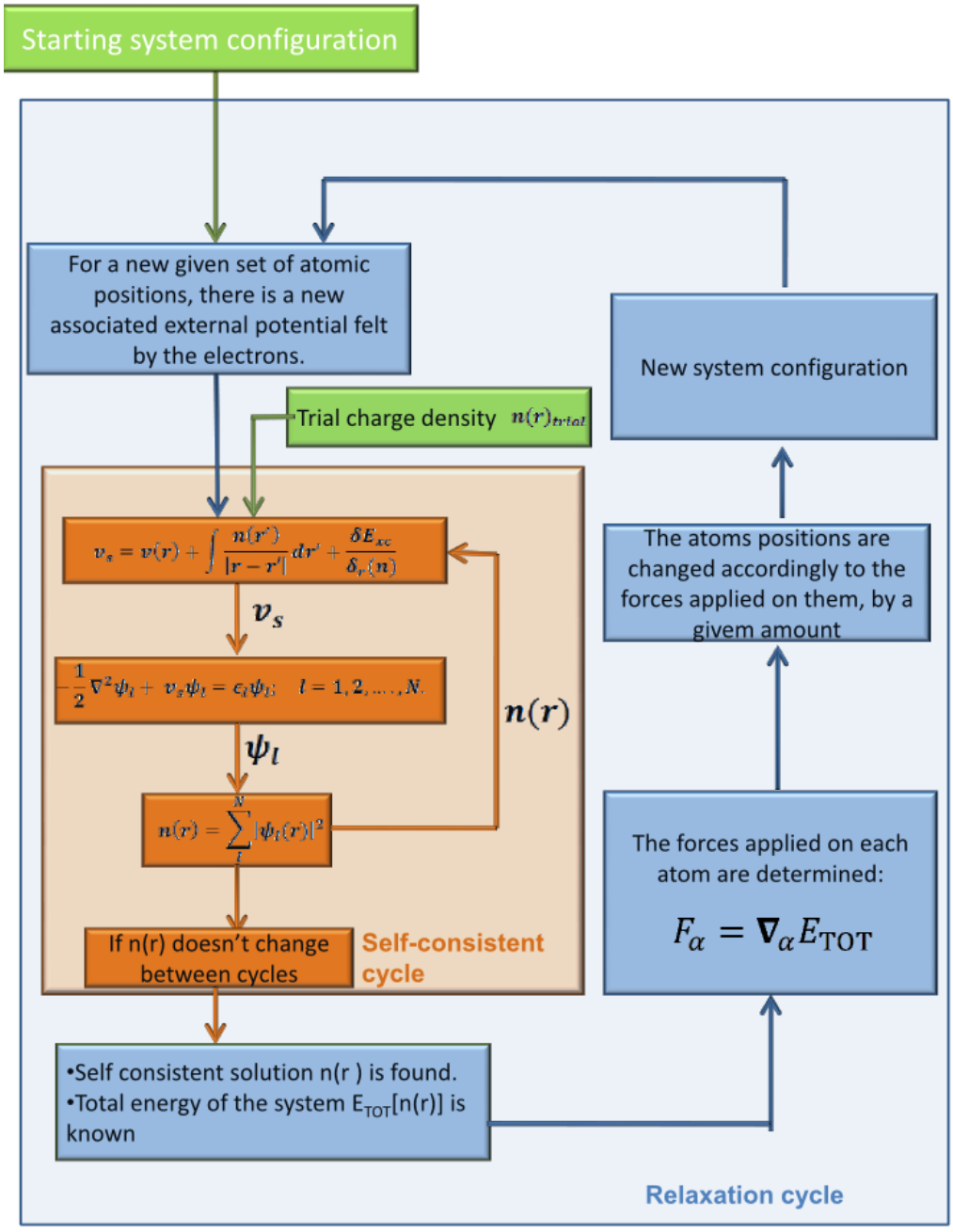

Figure 1.1: Schematic representation of the global structure optimization algorithm. The scheme depicts the inner self consistency cycle the outer structure optimization cycle and their interactions.

if a given hamiltonian $\hat{H}$ depends a parameter λ, and the respective expectable value of energy $\langle E \rangle$ at the state $\mid \psi \rangle$ is defined as:

$$\langle E \rangle = \langle \psi \mid \hat{H} \mid \psi \rangle, \tag{1.42}$$

then:

$$\frac{\partial E}{\partial \lambda} = \langle \Psi \mid \frac{\partial \hat{H}}{\partial \lambda} \mid \Psi \rangle. \tag{1.43}$$

Once the forces are known, the positions of the atoms are changed accordingly to the forces applied on them. For a given component $m = x, y, z$ of the force $\mathbf{F}_\alpha^n$ applied on the atom α at the iteration n, the conjugated direction $\mathbf{d}_\alpha^n$ whereby the atom is moved is given by:

$$\mathbf{d}_{\alpha m}^n = \mathbf{F}_{\alpha m}^n - x\mathbf{d}_{\alpha m}^{n-1}, \tag{1.44}$$

with:

$$x = \sum_{\alpha,m} \mathbf{F}_{\alpha m}^n (\mathbf{F}_{\alpha m}^n - \mathbf{F}_{\alpha m}^{n-1}) / \sum_{\alpha,m} (\mathbf{F}_{\alpha m}^{n-1})^2. \tag{1.45}$$

The new coordinates of the atom α become:

$$\mathbf{R}'_{\alpha m} = \mathbf{R}_{\alpha m} + w_\alpha^n \mathbf{d}_{\alpha m}^n, \tag{1.46}$$

where the parameter w_α^n is chosen in a way that the total energy is minimized. To make that choice, the AIMPRO code resorts to a cubic interpolation of the total energy and its directional derivative along $\mathbf{d}_\alpha^n$ between two points. The first point P_1 corresponds to a situation where the atom α is located at its starting position, whereas the second point P_2 corresponds to moving the atom by a fixed amount along the conjugated direction. Once the interpolation is done, the algorithm searches for the intermediate P_3 point that minimizes the total energy. The amount of distance covered from P_1 to P_3 along the conjugated direction gives us the value of w_α^n. Figure 1.1 presents a global view of the relaxation algorithm, including the electronic self consistent cycle, the atomic conjugated gradient relaxation and the interaction between both.

Reaction and transformation barriers: NEB method

The nudged elastic band (NEB) method is applied to determine saddle points of transformation paths between two stationary states (Henkelman *et al*, 2000). For instance, this method can be applied in the determination of migration barriers of defects in crystalline materials.

The method is based on a chain of *images* that constitute a discrete representation of the reaction path, with each image corresponding to an intermediary configuration of the defective supercell. These images are linked by a virtual elastic band that prevents them from collapsing into each other. The total force acting on each atom of a given image will take into account the elastic band force $\mathbf{F}_{\alpha,\parallel}^{\mathrm{s}}$, and is given by:

$$\mathbf{F}_\alpha = -\boldsymbol{\nabla}_\alpha E_{\mathrm{TOT},\perp} + \mathbf{F}_{\alpha,\parallel}^{\mathrm{s}}, \tag{1.47}$$

where $-\boldsymbol{\nabla}_\alpha E_{\mathrm{TOT},\perp}$ is the real force projected in the direction perpendicular to the elastic band:

$$-\boldsymbol{\nabla}_\alpha E_{\mathrm{TOT},\perp} = \boldsymbol{\nabla}_\alpha E_{\mathrm{TOT}} - (\boldsymbol{\nabla}_\alpha E_{\mathrm{TOT}} \cdot \mathbf{e}_{\alpha,i\parallel})\mathbf{e}_{\alpha,i\parallel}. \tag{1.48}$$

The unitary vector $\mathbf{e}_{\alpha,i\parallel}$ gives us the direction of the elastic band, that links two consecutive images, i and $i+1$:

$$\mathbf{e}_{\alpha,i\parallel} = \frac{\mathbf{v}_{\alpha,i\parallel}}{\mathrm{v}_{\alpha,i\parallel}} \tag{1.49}$$

.

with:

$$\mathbf{v}_{i\parallel} = \frac{\mathbf{R}_{\alpha,i} - \mathbf{R}_{\alpha,i-1}}{\mid \mathbf{R}_{\alpha,i} - \mathbf{R}_{\alpha,i-1} \mid} + \frac{\mathbf{R}_{\alpha,i+1} - \mathbf{R}_{\alpha,i}}{\mid \mathbf{R}_{\alpha,i+1} - \mathbf{R}_{\alpha,i} \mid}. \tag{1.50}$$

The elastic band force is parallel to $\mathbf{e}_{i\parallel}$ and comes as:

$$\mathbf{F}^{\mathrm{s}}_{\alpha,\parallel} = [k(\mid \mathbf{R}_{\alpha,i+1} - \mathbf{R}_{\alpha,i} \mid - \mid \mathbf{R}_{\alpha,i} - \mathbf{R}_{\alpha,i-1} \mid) \cdot \mathbf{e}_{\alpha,i\parallel}]\mathbf{e}_{\alpha,i\parallel}, \tag{1.51}$$

where k is the elastic constant of the band. The condition presented in Eq. 1.47 is applied in the relaxation algorithm, making sure that the each image finds its lowest possible energy while maintaining equal spacing to neighboring images. The image with highest energy will be the closest representation of the saddle point. The energy difference between the saddle point and the starting image gives us the energy barrier associated to the reaction path.

Mulliken analysis

The proper description of gap states produced by a point defect is a key element in the investigation of the electrical properties of that defect. Information about the localization of a given gap-state λ can be obtained either in a qualitative or quantitative way. A plot of the respective Kohn-Sham wave function can give us a qualitative insight on the shape, symmetry and localization of λ. However, when it comes to obtaining quantitative information about the gap-state, the analysis of Mulliken bond populations $p_\lambda(i)$(Pople and Beverage, 1970) is applied. The value of $p_\lambda(i)$ is directly related to the contribution of a given basis function ϕ_i to the gap-state:

$$p_\lambda(i) = \frac{1}{N_L} \sum_{j,\mathbf{k}} c_{\mathbf{k}\lambda,i} S^{\mathbf{k}}_{ij} c^*_{\mathbf{k}\lambda,j}, \tag{1.52}$$

where $S^{\mathbf{k}}_{ij}$ are the overlap matrix elements:

$$S^{\mathbf{k}}_{ij} = \int B^*_{\mathbf{k}i} e^{-\mathrm{i}\mathbf{k}.\mathbf{r}} \mathrm{B}_{\mathbf{k}j} d\mathbf{r}. \tag{1.53}$$

The sum of Eq. 1.52 is made over special $\mathbf{k}$ points, and $\sum_i p_\lambda(i) = 1$. The larger the value of $p_\lambda(i)$, the stronger the contribution of ϕ_i to λ will be. Since each basis function ϕ_i is centered in a particular atom, we can obtain a quantitative measure of the spatial localization of λ just by computing $p_\lambda(i)$ for all i. On the other hand, for hybrid states, we can estimate the contribution of s, p or d components, just by comparing $p_\lambda(i)$ for all s-, p- and d-type orbitals. The results of Mulliken bond population analysis can be compared to several types

of magnetic resonance data. For instance, we can apply the Mulliken bond population results in the LCAO analysis of the hyperfine structure, for a particular point defect.

Localized vibrational modes

Normal vibrational modes with frequencies above the Raman frequency are denominated as local vibrational modes (LVM's). The LVM's and their respective frequencies can be determined accurately with the aid of DFT based methods. Here, the total energy E of a N atom system is expanded to the second order, relatively to the atomic displacements (harmonic approximation) (Born and Huang (1954)):

$$E = E_0 + \frac{1}{2}\sum_{i,j}^{N} \mathbf{u}_i \cdot K(i,j) \cdot \mathbf{u}_j, \tag{1.54}$$

where E_0 is the static total energy, $\mathbf{u}_i$ is the displacement of the atom i. $K(i,j)$ is a rank 2 tensor, whose elements $K_{ab}(i,j)$ are usually referred to as force constants, and are given by:

$$K_{ab}(i,j) = \frac{\partial^2 E}{\partial u_{i,a} \partial u_{j,b}}, \tag{1.55}$$

where the indexes a and b stand for any of the three Cartesian coordinates.
These matrix elements can be obtained with the aid of the AIMPRO code, which can check the variation of the total energy with the atom motion, thus being able to calculate its second derivatives.

Now we can write down the equation of motion for an atom i with mass M_i

$$M_i \frac{\partial^2 \mathbf{u}_i}{\partial t^2} = -\boldsymbol{\nabla}_i E = -\sum_{j}^{N} K(i,j) \cdot \mathbf{u}_j. \tag{1.56}$$

The dependence of the atomic displacement over time $\mathbf{u}_i(t)$ can be assumed as oscillatory, and the previous equation can be re-writen as an eigenvalue problem:

$$D.\mathbf{U} = \omega^2 \mathbf{U}, \tag{1.57}$$

where D is a $3N \times 3N$ matrix, usually called *dynamical matrix*. Its elements are given by:

$$D_{ab}(i,j) = \frac{1}{\sqrt{M_i M_j}} K_{ab}(i,j). \tag{1.58}$$

By solving this eigenvalue problem we obtain $3N$ eigenvalues ω^2 which are the square frequencies associated to the $3N$ normal modes. When we deal with periodic systems, the summations above are made over the atoms of the unit cell and over all the unit cells. With that purpose we add a new index l representing the number of the cell. Hence, the displacement of the $i-th$ atom in the $l-th$ cell will be given by $\mathbf{u}_{il}$. The Equation 1.56 becomes now a wave equation. The force constants are now written as $K(il, jl')$, and the matrix elements of the dynamical matrix for a unit cell become:

$$D^{\mathbf{k}}_{ab}(i,j) = \frac{1}{\sqrt{M_i M_j}} \sum_{l} K_{ab}(i0, jl) e^{\mathbf{i}\mathbf{k}.(\mathbf{r}_{jl} - \mathbf{r}_{i0})}. \tag{1.59}$$

By comparing Eqs. 1.58 and 1.59 we can see that a phase factor depending on the equilibrium position of atoms r_{il} was added. Associated to that is the introdution of a new set of quantum numbers represented by the vector $\mathbf{k}$.

Electrical levels, the marker method

The transition energy between two consecutive charge states (also called electrical level) of a particular defect in a solid is another type of observable that can be predicted with the aid of DFT methods, and it is easily compared to experimental data, more specificaly, DLTS measurements. Nevertheless, there are some errors associated to the calculations that must be taken into account. There are two main reasons behind these errors: defect-image interactions in supercell calculations (see Section 1.6.2: structure optimization) and underestimation of the gap when the LDA functional is applied. There are several approaches that can be used to avoid these errors. In this work we apply the *marker* approach (Coutinho *et al*, 2003), which involves using a defect that is well established experimentally as a benchmark for our calculations. The marker method basically assumes that, for two consecutive charge states q and $q+1$, the off-set between ionization potentials/electron affinities for the defect under scrutiny $I_{\mathrm{d}}(q/q+1)$ and the marker defect $I_{\mathrm{m}}(q/q+1)$ is approximately same as the off-set between the respective experimental levels, i.e.

$$I_{\mathrm{d}}(q/q+1) - I_{\mathrm{m}}(q/q+1) \approx E_{\mathrm{d}}(q/q+1) - E_{\mathrm{m}}(q/q+1), \tag{1.60}$$

Then, the electrical level of the defect under scrutiny simply becomes:

$$E_{\mathrm{d}}(q/q+1) \approx I_{\mathrm{d}}(q/q+1) - I_{\mathrm{m}}(q/q+1) + E_{\mathrm{m}}(q/q+1), \tag{1.61}$$

where $E_{\mathrm{d}}(q/q+1)$ and $E_{\mathrm{m}}(q/q+1)$ are the transition energies between the charge states q and $q+1$ for the defect at study and the marker defect, respectively. The acuracy of this approximation is deeply related to the degree of similarity between shapes and localization between the acceptor (and donor) states of both defects. If the defect under scrutiny and the marker defect produce states in the gap that are similar enough, the errors in the calculations will practically cancel each other in Eq 1.62. We must also ensure that the calculations are made in the same conditions (supercell size, basis functions, pseudo potentials, etc). Since the value of the transition energy $E_{\mathrm{m}}(q/q+1)$ is known from measurements, we just have to calculate the ionization potentials $I_{\mathrm{d}}(q/q+1)$ and $I_{\mathrm{m}}(q/q+1)$. These ionization potentials are given by:

$$I(q/q+1) = E_q[\mathbf{R}] - E_{q+1}[\mathbf{R}], \tag{1.62}$$

where $E_q[\mathbf{R}]$ and $E_{q+1}[\mathbf{R}]$ are the total energies of a system with configuration $\mathbf{R}$ for the charge states q and $q+1$ respectively. An analogous reasoning is applied for electron affinities. Therefore, according to Eq 1.62, we obtain:

$$\begin{aligned} I_{\mathrm{m}}(q/q+1) &= E_q[\mathbf{R}_{\mathrm{m}}] - E_{q+1}[\mathbf{R}_{\mathrm{m}}] \\ I_{\mathrm{d}}(q/q+1) &= E_q[\mathbf{R}_{\mathrm{d}}] - E_{q+1}[\mathbf{R}_{\mathrm{d}}], \end{aligned} \tag{1.63}$$

where $\mathbf{R}_{\mathrm{m}}$ and $\mathbf{R}_{\mathrm{d}}$ correspond to a defective supercell that includes our marker defect or the defect under scrutiny, respectively. These calculations are performed by adding electrons to the Highest occupied Kohn-Sham (HOKS) level and place a uniformly positivey charged

background *jellium* that assures the charge neutrality of the supercell for negative charge states. For positive charge states we remove electrons from the Lowest unoccupied Kohn-Sham LUKS level and apply a negative *jellium*. In some particular cases, where there are suitable defects to be used as a marker, we use the bulk material itself as a benchmark. In that case $E_m(q/q+1)$ is replaced by the energy of the conduction band E_c or valence band E_v for $q <$or $q \geq 0$ respectively.

Chapter 2

Multivacancy clusters in silicon

This chapter is based on the work published in P. Santos, J. Coutinho, M. J. Rayson and P. Bridon, *Physica Status Solidi*, **9**, 2000 (2012)

2.1 Introduction

The degradation of silicon detectors when exposed to several types of radiation is a significant issue in particle detection applications such as medical imaging or in fundamental science like in high-energy physics (Dierlamm, 2010). This degradation is related to the electrical activity of some structural point defects like vacancies or interstitial atoms (and their related aggregates), which are a direct product of the exposure to a radiation source. This is the case of the single Si vacancy (V) (Watkins, 1992), and also of some small multivacancy clusters (Lee and Crobett, 1974).

Early Electron Paramagnetic Resonance (EPR) and annealing studies by Lee and Corbett established a connection between specific paramagnetic signals with the production, transformation and annealing temperatures of the simplest vacancy clusters. The levels of the most elemental vacancy aggregate - the divacancy - were also early established. From Deep Level Transient Spectroscopy (DLTS), we know that in n-type Si it produces two prominent peaks related to first and second acceptor levels at $E_c - 0.42$ eV and $E_c - 0.23$ eV (Svensson *et al*, 1991), whereas in p-type material it has a hole trap related to a donor level at $E_v + 0.20$ eV (Trauwaert *et al*,1995). For a long period of time the electrical activity of the trivacancy and larger vacancy clusters was a matter of speculation, and much of the work relied on the above mentioned EPR data. More recently, concurrent work at Brunel (Ahmed *et al*, 2001) and at the CERN (Moll et all 2002) unveiled the first leads for the electrical activity of larger vacancy complexes. Accordingly, two deep electron traps at $E_c - 0.45$ eV and $E_c - 0.35$ eV were linked to the Si trivacancy and another trap at $E_c - 0.37$ eV was tentatively connected to the Si tetravacancy (V_4). Their activation barriers for annealing out of about 1 eV are slightly smaller than the 1.4 eV barrier for migration of V_2 (Watkins and Corbett, 1965), and since the divacancies anneal out by being trapped at donors or oxygen upon diffusion (and not by capturing mobile interstitial impurities), it is likely that the measured barriers correspond to migration or rearrangement mechanisms.

Structural and electrical properties of small vacancy aggregates in Si are still a subject of debate. The traditional atomic models for these defects comprise a family referred as Part-of-Hexagonal-Ring (PHR) structures (Chadi and Chang, 1988), where a given V_n complex

(with $n \leq 6$), is obtained by placing $6-n$ Si atoms at the vacant sites of a hexavacancy. The latter is obtained by removing an hexagonal ring of Si atoms in the lattice. This is depicted in Figs.2.1-d) and 2.1-f), where V_5 and V_4 have respectively one and two additional Si atoms (shown in green) when compared to V_6. Of special relevance is the fact that in V_6 all 12 Si dangling bonds that result from atom removal, reconstruct pairwise to form 6 long bonds [see green bonds in Fig.-2.1-b)], conferring to this defect great stability, and according to previous calculations (Hastings *et al*, 1997; Hourahine *et al*, 2000), no electrical activity. Conversely, PHR complexes possess highly reactive under-coordinated Si radicals (green atoms), responsible for two dangling bonds and higher formation energies (Chadi and Chang, 1988).
More recently, alternative and more stable configurations for V_n ($3 < n < 5$) were proposed by Makhov and Lewis (Makhov and Lewis, 1995). In these configurations, the $6-n$ Si atoms in excess to those in V_6 are displaced towards interstitial positions, in a way that each of them binds to four Si radicals edging the hexavacancy cage. These are shown in Figs. 2.1-c) and 2.1-e) for the cases of V_5 and V_4, respectively, where green Si atoms saturate four and eight dangling bonds around the hexagonal vacant ring, respectively. Analogously to V_6, the remaining dangling bonds form long Si-Si reconstruction pairs. These configurations are known as Four-Fold-Coordinated (FFC) and formation energies of FFC V_3, V_4 and V_5 were found below those of PHR counterparts by 0.6 eV, 1.1 eV and 0.7 eV, respectively. Also importantly, all FFC defects were predicted to be electrically inert. This picture was supported by the four-fold coordination of all atoms, but it is now clashing with the DLTS data assigned to V_3 and V_4 electron traps in n-type Si (Ahmed *et al*, 2001; Moll *et al*, 2002).
Actually in the case of the trivacancy, recent DLTS measurements combined with density functional calculations demonstrated that FFC V_3 is in fact electrically active with an acceptor level at $E_c - 75$ meV (Markevich *et al*, 2000). This paper is especially relevant as it shows that both PHR and FFC V_3 defects are formed, the transformation between them can be cycled upon annealing and current injection treatments, but also suggests that larger FFC complexes could be electrically active as well. This bi-stability of V_3 is only possible if there are high enough barriers preventing defect transformation above room temperature. We note however that the existing calculations indicate that the transformation barrier that separates V_5(FFC) from V_5(PHR) is estimated to be bellow 50 meV (Makhov and Lewis, 2004), and unlike V_3(PHR) the V_5(PHR) structure should not hold at room temperature with the FFC structure being readily formed. These are among the issues that we want to address in this chapter, and this can only be done by scrutinizing the charge dependent stability and the electrical activity of these complexes.

2.2 Method

To model a particular multivacancy cluster V_n we built a $512-n$ silicon cubic supercell. The Kohn-Sham states were expanded using a Cartesian-Gaussian basis set comprising 28 independent $s-$, $p-$ and $d-$ like orbitals per atom. The value of the cut-off energy radius E_{cut} for the charge density expansions in the reciprocal space was 80 Ry. The Brillouin Zone sampling was made at $\mathbf{k} = \Gamma$. The relaxation cycle was carried out until the total energy and atom position variations dropped below 0.3 meV and 5.0×10^{-5} Å respectively. Under these conditions, the lattice constant and bulk modulus of Si were respectively a_0=5.3947 Å and $B = 98.3$ GPa, in good agreement with their respective experimental values, $a_{0,\text{exp}} = 5.431$ Å and $B_{\text{exp=97.9}}$ GPa (Mohr and Taylor, 2000).

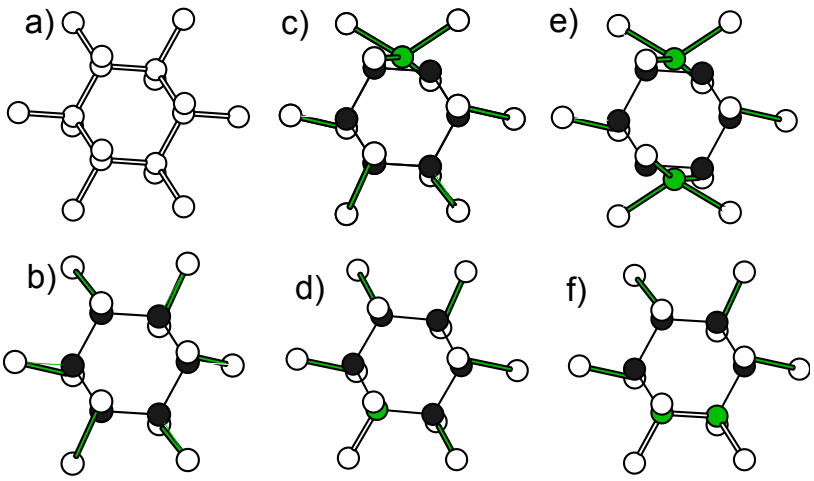

Figure 2.1: Atomic structure representation in the $\langle 111 \rangle$ view direction of: a) perfect crystaline Si region, and ground state structures of b) hexavacancy, c) FFC V_5 d) PHR V_5 e) FFC V_4 f) PHR V_4. The C_2 axis referred in the text concerning the description of the PHR V_5 and V_4 localized states is located in the hexagonal ring plane, intersecting the green atom in d) and the middle point between the two green atoms in f)

The formation energies $E_\mathrm{f}[\mathrm{V}_n]$ of a given multivacancy V_n were determined with the application of the following equation:

$$E_\mathrm{f}[\mathrm{V}_n] = E[\mathrm{V}_n] - (N-n)\mu_\mathrm{Si}, \tag{2.1}$$

where $E[\mathrm{V}_n]$ is the total energy of the defective supercell made of $N-n$ atoms, and μ_Si the chemical potential of Si taken as the energy per atom from a pristine supercell made of $N = 512$ atoms, $\mu_\mathrm{Si} = E[\mathrm{pristine}]/N$. Electrical levels were estimated with the marker method, where a bulk supercell was taken as the marker reference.

2.3 Results

2.3.1 Formation energies and stability

Our calculations confirm that neutral FFC structures are stable and have lower formation energies than PHR counterparts. Accordingly, their total energy was lower than that of PHR structures by 1.25 eV and 0.62 eV for V_4 and V_5, respectively. We also confirmed that the PHR sctructures are stable. However, when a simmetry distortion is applied (by dislocating one or more of the remaining atoms), the PHR form of V_5, which has C_{1h} point group symmetry, spontaneously relaxes to the lower energy FFC form (C_2 point group symmetry). That is not the case of PHR V_4, which remained stable upon symmetry distortion. These results suggest that even if for kinetic reasons PHR structures are primarily formed upon irradiation, V_5 FFC defects will be readily formed even at cryogenic temperatures. The

Table 2.1: Formation energies E_f in eV for tetra, penta and hexavacancy in FFC and PHR configurations. Calculations from Makhov and Lewis (2004) are shown for comparison (braced values). The structure stability analysis is also summarized

	symmetry point group	E_f	stability upon symmetry distortions
V_4(PHR)	C_2	8.74(8.35)	structure remains stable
V_4(FFC)	C_{2h}	7.49(7.26)	structure remains stable
V_5(PHR)	C_{1h}	9.35(9.07)	structure relaxes to FFC form
V_5(FFC)	C_2	8.73(8.42)	structure remains stable
V_6	D_{3d}	9.64(9.43)	structure remains stable

overall results about formation energies and stability are summarized in Table 3.1
The relative stability between different sized aggregates was also investigated. We found that, as we consecutively remove silicon atoms from the hexagonal ring, the ratio between formation energy and n becomes lower, reaching its minimum value at $n = 6$. The results are ploted at figure 2.2 and clearly demonstrate that small vacancy clusters $n < 6$ have a tendency to aggregate.

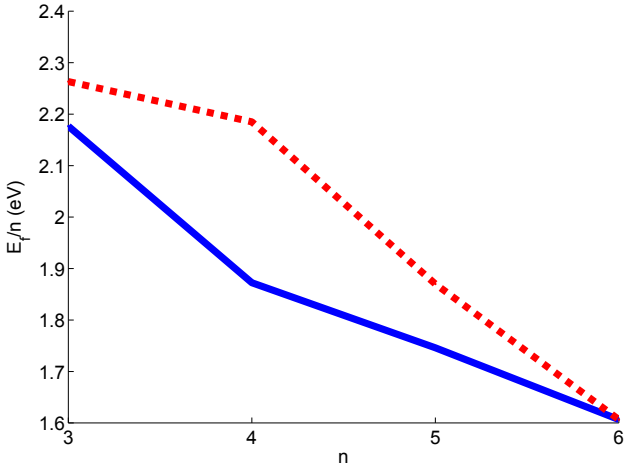

Figure 2.2: Plot of the ratio $E_f[V_n]/n$ versus n. The FFC and PHR structures are represented by the blue solid line and red dashed line respectively.

2.3.2 Gap states and electrical activity

Density functional Kohn-Sham states are not one-electron states but rather eigenvectors from the Kohn-Sham equations. Despite that, their shape, localization and symmetry are often used to understand the character of donor and acceptor states. Inspection of $\psi_{k,\lambda}$ Kohn-Sham states at levels λ within the gap and at $k = \Gamma$ allow us to understand the stability and electrical activity of these complexes. Although several levels are found within the gap, we restrict our analysis to the highest-occupied and lowest-unoccupied Kohn-Sham states (HOKS and LUKS, respectively). The states are labeled with the respective representation label of the symmetry group of the defect, see Tables 2.4, 2.3 and 2.4 for more details. We start describing V_6 since the other complexes inherit many of its electronic properties. While the HOKS is a valence band type state, the LUKS level (see Fig 2.3) is a deep a_{1u} state close to mid-gap (only 10 meV below the a_{1g} level), and is made of a linear combination of anti-bonding states between the elongated bonds shown in green in Fig.2.1-b). This result is at variance with previous calculations (Hastings *et al*, 1997; Hourahine *et al*, 2000) and questions the rather established idea that V_6 is electrically inert. Before exploring this avenue, let us have an outlook of PHR V_4 and V_5 structures. These defects have HOKS and LUKS states localized on Si dangling bonds (symmetric and anti-symmetric states with respect to the C_2 axis and mirror plane, respectively). In V_5 this arises from the two-fold coordinated Si atom, whereas in V_4 they are located on two three-fold coordinated Si atoms [shown in green in Figs 2.1-c) and 2.1-e)]. States arising from the elongated bonds (with V_6 character) are closer to the band edges and should not play a relevant role on their electrical activity.

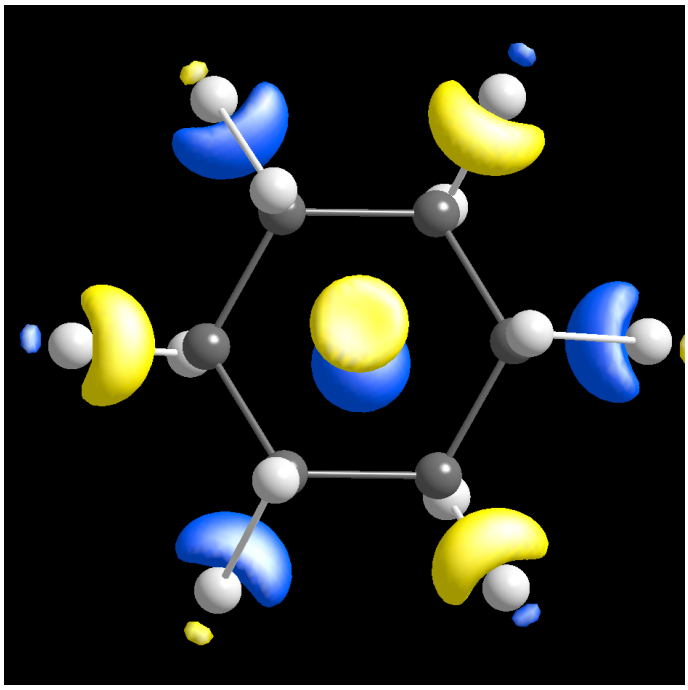

Figure 2.3: Representation of the a_{2u} Kohn Sham state of V_6. It Comprises anti-bonding states in all of the reconstructions.

	E	$2C_3$	$3C_2$	i	$2S_6$	$3\sigma_d$
a_{1u}	1	1	-1	-1	-1	1
a_{1g}	1	1	1	1	1	1

Table 2.2: Reduced character table of the D_{3d} symmetry group, corresponding to the observed gap states of the V_6 defect

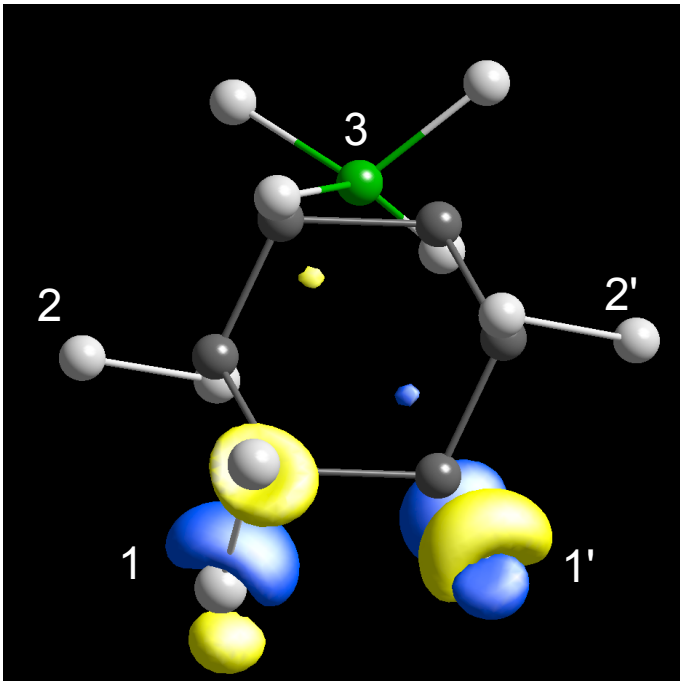

Figure 2.4: Representation of the a Kohn Sham state of V_5. Anti-bonding states related to the reconstructions at 1 and 1'. The Kohn Sham state associated to the b representation is lower in energy and comprises anti-bonding states at 2 and 2' with an interstitial Si state at 3

	E	C_2
a	1	-1
b	1	1

Table 2.3: Reduced character table of the C_2 symmetry group, corresponding to the observed gap states of the V_5 defect

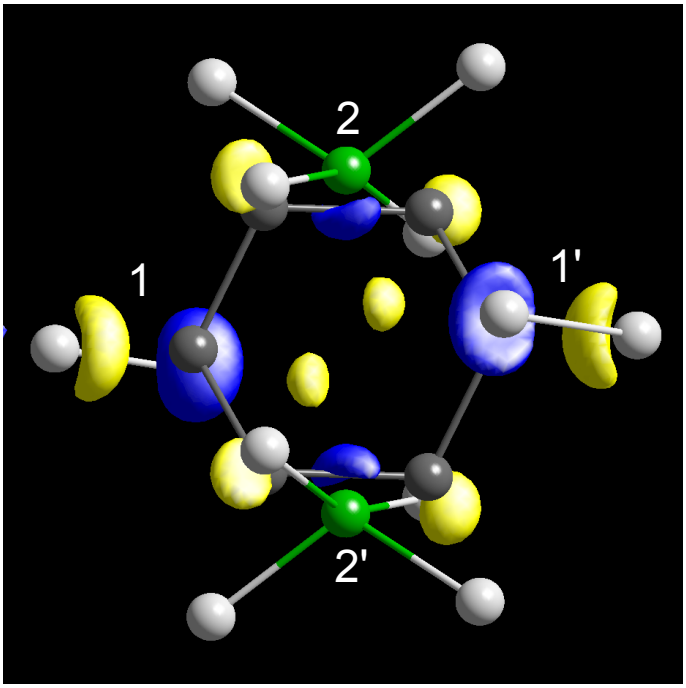

Figure 2.5: Representation of the a_g Kohn Sham state of V_4. Anti-bonding states related to the reconstructions at 1 and 1'. Interstitial Si states at 2 and 2'

	E	C_2	σ_h	i
a_g	1	1	1	1

Table 2.4: Reduced character table of the C_{2h} symmetry group, corresponding to the observed gap states of the V_4 defect

By removing one electron from the HOKS level and placing that on a uniformly charged background *jellium* we can represent a positively charged defect with a localized donor state. We found that under these conditions, supercells containing FFC V_4 and V_5 are more stable than those with PHR structures by 0.99 eV and 0.63 eV (total energies). Conversely by adding one electron to the LUKS level (and a positive *jellium* background) to represent negatively charged states we found that cells containing FFC V_4 and V_5 are more stable than those with PHR structures by 1.05 eV and 0.62 eV, respectively. This picture is similar for doubly positive and doubly negative cells as well. Applying these same conditions we also investigated the stability of charged defects, when small symmetry distortions are introduced. Once again, the PHR form of the pentavacancy spontaneously relaxed to its FFC counterpart. All other considered structures appeared to remain stable after relaxation. We note that these results by themselves do not gives all the information about the stability of charged multivacancy defects. To this end we need to calculate their electrical levels (Table 2.5).

	$E(-/0)$	$E(-/--)$	$E(0/+)$	$E(+/++)$
V_4(FFC)	$E_c - 0.54$	$E_c - 0.54$	-	-
V_4(PHR)	$E_c - 0.71$	$E_c - 0.73$	$E_v + 0.25$	$E_v + 0.21$
V_5(FFC)	$E_c - 0.45$	$E_c - 0.47$	-	-
V_6	$E_c - 0.36$	$E_c - 0.34$	-	-

Table 2.5: Electrical levels calculated with the Marker method for the tetra, penta and hexa vancancies stable configurations in silicon.

Our results show the existence of electrical activity in all of the considered multivacancy agregates, for both FFC and PHR configurations. While V_6 has first and second acceptor levels at around 0.35 eV below E_c, the Si radicals in PHR V_4 are responsible for rather deep first and second acceptor levels at about 0.7 eV below E_c. It is possible however that due to the underestimation of the correlation potential within LDA the depth of the calculated acceptor levels (with respect to E_c) could be overestimated. We also looked at donor levels and while these were not found in V_6, the calculations indicate that PHR V_4 has first and second donor levels at about 0.2 eV above E_v. This result is consistent with defects possessing dangling bonds, and are close to similar levels found for PHR V_3 (Markevich *et al*, 2009).
Now we look at FFC structures. In V_5 and V_4, some empty elongated bond states present in V_6 are removed or displaced upwards in the gap due to the introduction of one and two four-fold coordinated Si atoms, respectively. Like in V_3 [(Markevich *et al*, 2009), states localized on FFC Si atoms of V_4 and V_5 are edging the conduction band bottom. The LUKS states, shown in Figs. 2.5 and 2.4, are mostly localized on the elongated bonds and are very similar to the LUKS level in V_6. No bound HOKS levels were found for these structures. Electrical levels for FFC V_4 and V_5 are reported on Tab. 2.5 and confirm that these structures do not introduce donor states in the gap but rather they are predicted to be double acceptors. The FFC Si atoms in V_4 and V_5 open the V_6 cage, slightly increasing the length of the elongated bonds and deepening their associated states. This is why both first and second acceptor levels of V_4 lie at about E_c-0.54 eV and for V_5 they are predicted at about $E_c - 0.45$ eV (closer to the acceptor levels of V_6). This location is consistent with the detection in heavily irradiated Si of several DLTS levels superimposed to the $V_2(-/0)$ signal at $E_c - 0.42$ eV, and assigned to multivancancy complexes (Ahmed *et al*,2001; Moll *et al*, 2002).

Since the tetravacancy seems to admit two stable configurations in all the considered charge states, we built its formation energy diagram. The formation energy $E_f[\mathbf{R}_d^q](\mu_e)$ of a given defect represented by a configuration R in the charge state $q > 0$, can be estimated with the application of following equality(Coutinho *et al*, 2003):

$$E_f[\mathbf{R}_d^q](\mu_e) = E_f[\mathbf{R}_d^{q-1}] + q\mu_e - q[I_d(q - 1/q) - I_m(q - 1/q)]. \quad (2.2)$$

Analogously, for a negatively charged state $q < 0$, it becomes:

$$E_f[\mathbf{R}_d^q](\mu_e) = E_f[\mathbf{R}_d^{q+1}] + q\mu_e - q[I_d(q/q + 1) - I_m(q/q + 1)]. \quad (2.3)$$

From equations 2.2 and 2.3 we obtained $E_f[\mathbf{R}_d^q]$ for $-2 < q < 2$ for both PHR and FCC

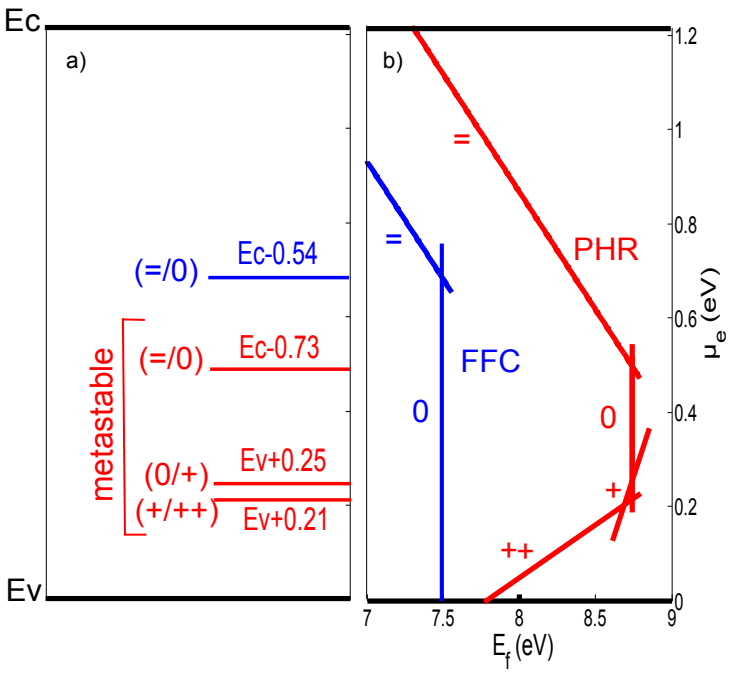

Figure 2.6: Calculated electrical level diagram (a) and formation energy diagram (b) for the tetra-vacancy

configurations of the tetravacancy. The result is represented in the formation energy diagram depicted in fig 2.6.

The diagram confirms the FFC form to be the most stable for any location of the Fermi level μ_e in the gap.

2.4 Conclusions

We presented density functional calculations of structural and electronic properties of small vacancy clusters in Si. It is confirmed that neutral FFC structures of V_4 and V_5 are more stable than PHR structures. This stability order is also shown for charged complexes (from doubly positive to doubly negative charge states). While the electrical activity of PHR structures arises from under-coordinated Si radicals, the FFC forms have acceptor levels localized on elongated bonds similar to those in V_6. Acceptor level pairs at about 0.54 eV, 0.46 eV and 0.35 eV below E_c are predicted for FFC V_4, FFC V_5 and V_6 defects, respectively.

Chapter 3

The oxygen dimmer in Si and its relationship to the light-induced degradation of Si solar cells

Some results of this chapter were published in L. I. Murin, E. A. Tolkacheva, V. P. Markevich, A. R. Peaker, B. Hamilton, E. Monakhov, B. G. Svensson, J. L. Lindstrm, P. Santos, J. Coutinho, and A. Carvalho, *Applied Physics Letters*, **98**, 182101 (2011)

3.1 Introduction

Nowadays, silicon solar cells represent around 90% share of the solar cell market (Taishi *et al*, 2007). Amongst a wide variety of options, monocrystaline n^+p silicon cells are the most common ones, reaching efficiencies up to 25% (Zhao *et al*, 1998).
Boron-doped Czochralski(Cz)-grown silicon can potentially offer highly competitive ratio between efficiency and price when it comes to mass production of n^+p-type solar cells. However, when exposed to light, they suffer a relative 10% degradation in their efficiency (Bothe and Schmidt, 2006). The very same effect also occurs upon the injection of minority carriers in the n^+p junction. This issue is directly related to the high concentration of oxygen impurities that are present in Cz-Si([O_i]$\approx 10^{-18}$ cm$^-$3) (Cleland,1982), being less noticeable in crystalline silicon produced with more expensive growth techniques like floating zone (FZ) method, with lower oxygen concentrations. The efficiency-degradation problem in boron doped Cz-Si occurs in two sequential stages: a fast but moderate stage (in the time scale of minutes) followed by a slow but strong one (asymptotic decay up to 10% relative efficiency, in the time scale of few hours) (Bothe and Schmidt, 2006). Both stages are deeply related to the formation of recombination centers as a consequence of either the exposure of the junction to the light or minority carrier injection. These recombination centers are able to produce deep gap states, working as traps for minority charge carriers. From now on we shall focus on the slow-forming recombination center (and label it as SRC), associated to the second degradation stage. Injection-level dependent carrier-lifetime measurements place a SRC-related trap level in the region between $E_v + 0.35$ eV and $E_c - 0.45$ eV (Schmidt and Cuevas, 1999). Advanced lifetime spectroscopy pinned down the level to $E_v + 0.41$ eV (Rein and Glunz, 2003). The concentration of the trap was found to be proportional to the concentration of substitutional boron [B_s](Glunz *et al*, 1998) and to the square of the concentration of interstitial oxygen

[O_i] (Schmidt *et al*, 2002). These results confirm the required presence of boron dopants and high concentrations of oxygen for the degradation to occur. Another important finding about these SRCs is that they anneal out in the dark at 200° C with an activation energy of 1.3 eV (Rein *et al*, 2001; Bothe *et al*, 2003).
In view of these results, some theoretical models concerning the constitution, structure and formation mechanisms of the SRCs have been suggested. One of the most discussed models in the literature is the B_sO_{2i} model proposed by Schmidt *et al*. The model assumes that, in the presence of charge carriers and light, the existing interstitial oxygen dimmers O_{2i} in the material assume a fast diffusing configuration O^*_{2i} that can be trapped by several other impurities like single interstitial oxygen atoms O_i or substitutional boron atoms B_s, resulting in the formation of new complexes like the O_{3i} oxygen aggregate or the B_sO_{2i} defect. This last one is assigned to the slow-forming recombination center we look for.
The B_sO_{2i} model requires the existence of two or more stable forms of the oxygen dimmer in silicon, one of them able to diffuse in the material at room temperature, under the aforementioned efficiency degradation conditions. In fact, first principles calculations (Adey *et al*, 2004) predict a charge driven bi-stability of the O_{2i}, with a stable form in the neutral charge state, [from now on labeled as Staggered (St) Fig. 3.1-a)] and in the double positive charge state (labeled as Squared (Sq) form, Fig. 3.1-b)). The transition between the two configurations was predicted to occur when the Fermi level is at about $\mu_e = E_v + 0.40$ eV. The reconfiguration energy barriers that stand between them were also estimated for the neutral, positive and double positive charge states. The results show a high 0.86 eV barrier associated to the O_{2i}^{sq++} to O_{2i}^{st++} reaction path. The activation energy of the reverse process is only 0.3 eV. This 0.86 eV barrier seems to rule out the possibility of diffusion of the oxygen dimmer in p-type silicon at room temperature. However, under illumination or electron injection, the O_{2i}^{sq++} is able to trap an electron, becoming single positively charged, and migrate to a metastable O_{2i}^{st+} configuration, with an estimated energy barrier of 0.2 eV[fig 3.1 b)]. Subsequently, the defect emits an electron, becoming double positively charged once again, in the staggered form. [Fig. 3.1-d)]. Finally, by overcoming the 0.3 eV energy barrier, the dimmer returns to the O_{2i}^{sq++} configuration, resetting the process [Fig. 3.1-a)]. This is a typical example of a Bourgoin-Corbett (1972) migration mechanism, leading to dimmer-diffusion energy of only 0.3 eV, which is achievable under the degradation conditions. The Coulombic attraction between the mobile O_{2i}^{++} aggregate and the substitutional boron B_s^- would enhance the possibility of formation of the B_sO_{2i} complex.
Nevertheless, despite the theoretical modeling predictions, there is not yet clear evidence that supports the existence of O_{2i}^{st++} form of the dimmer. In the next chapter we present first principle calculations concerning the electrical activity and localized vibrational modes(LVMs) of the dimmer as well and infrared spectroscopy data recorded by our collaborators at the University of Manchester, UK.

3.2 Method

To model this particular defect we built supercells containing 216 silicon atoms and 2 oxygen atoms. The Brillouin-Zone sampling and convergence criteria used are the same as the ones mentioned in the previous chapter. We use a total 40 Gaussian basis functions to expand the Kohn-Sham states nearby the oxygen atom.
We applied the marker method to determine the electrical levels and calculated the formation

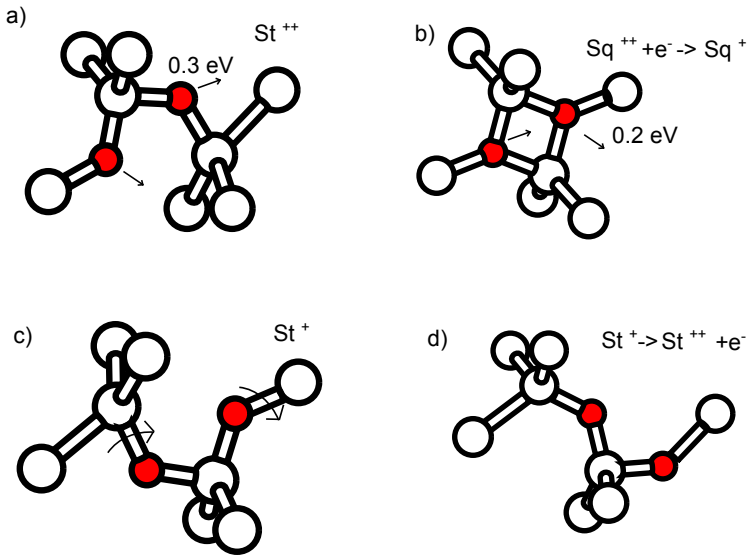

Figure 3.1: Representation of the Bourgoin-Corbett migration mechanism. a) transition from O_{2i}^{st++} to O_{2i}^{sq++} with a barrier of 0.3 eV. b) the dimmer in the squared configuration captures and electron and becomes single positively charged O_{2i}^{sq+}, and migrates to the O_{2i}^{st+} form with an energy barrier of 0.2 eV. c) rotation of the oxigen atoms in the staggered configuration relatively to the Si-Si axis of the Si-O-Si group. d) O_{2i}^{st+} emits an electron, and the process restarts.

energy diagram for the oxygen dimmer. For this particular case, the formation energy of the defect in the configuration Ω in the charge state q is given by:

$$E_{\rm f}[\Omega^{\rm q}] = E[\Omega] - n\mu_{\rm Si} - 2\mu_{\rm O} - q\mu_{\rm e}, \tag{3.1}$$

where $E[\Omega]$ is the total energy of the defective supercell containing n silicon atoms and 2 oxygen atoms. However, since we are only interested in the relative stability between different configurations, we will work with energy differences, thus avoiding the determination of $\mu_{\rm O}$ and $\mu_{\rm Si}$. For instance, when comparing the formation energies between the squared and staggered configurations in the neutral charge state we obtain:

$$\begin{aligned} E_{\rm f}[{\rm Sq}] - E_{\rm f}[{\rm St}] &= E[{\rm Sq}] - n\mu_{\rm Si} - 2\mu_{\rm O} - (E[{\rm St} - n\mu_{\rm Si} - 2\mu_{\rm O}) = \\ &= E[{\rm Sq}] - E[{\rm St}]. \end{aligned} \tag{3.2}$$

Which is simply the difference between total energies of the defective supercells containing the oxygen dimmer in the respective configuration.
We determined the LVMs by diagonalizing the dynamical matrix. Relative LVM intensities were obtained from effective charges localized in the Oxygen atoms and their Silicon first neighbours. The intensity of the mode is then proportional to the squared change in the dipole moment of the defect when the atoms are displaced according to their mass weighted normal coordinates. Our collaborators have carried out infrared IR absorption measurements

on several of n- and p-type Cz-Si crystals with different doping levels and oxygen content including materials with identical doping and oxygen content to those in which light induced degradation attributed has been observed. The details are presented in the captions of Figs. 3.3 and 3.4). The IR absorption spectra have been measured at 300 K and at $\approx 15K$ in the frequency range 400-4000 cm^{-1} with the use of Bruker IFS113v spectrometer.

3.3 Results

3.3.1 Structures and stability, Electrical levels

We computed the total supercell energies and relative formation energies for the neutral, positively charged and doubly positive charged states of the oxygen dimmer. Our calculations confirm that the staggered configuration is the most stable one in the neutral and positively charged states, with total supercell energies that lie 1.31 eV and 0.46 eV below the ones corresponding to the neutral and positively charged squared form of the dimmer, respectively. Moreover, in the neutral charge state, when small symmetry distortions are applied to the squared form of the dimmer, it will spontaneously relax to its staggered form. However, at doubly positive charged state the situation is reversed, and the squared structure O_{2i}^{sq++} becomes the most stable. We obtained an energy difference between O_{2i}^{sq++} and O_{2i}^{st++} configurations of 0.7 eV.
Following an analogous reasoning as in Section 2.3.2, Eqs. 2.2 and 2.2, we built the formation energy diagram for the oxygen dimmer, presented in Figure 3.2. This diagram clearly shows the bi-stable behaviour of the defect, which can assume two possible stable configurations, O_{2i}^{st0} or O_{2i}^{sq++}, accordingly to its charge state. We also suport previous calculations (Adey *et al*, 2004) that predict the O_{2i} to be a double donor, with a $(0/++)$ electrical level located at $E_v + 0.47$. These globally confirm the bi-stability and double donor nature of the O_{2i} defect which is considered in the literature as strong supportive argument for the formation of the B_sO_{2i} recombination center via Bourgoin-Corbett migration mechanism of the dimmer.

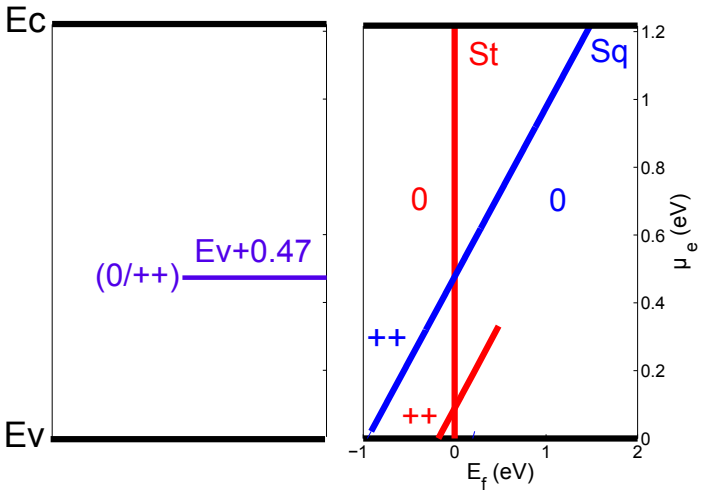

Figure 3.2: Calculated electrical level diagram (a) and formation energy (E_f) diagram as a function of the electron chemical potential (μ_e)(b) for the O_{2i} defect in silicon.

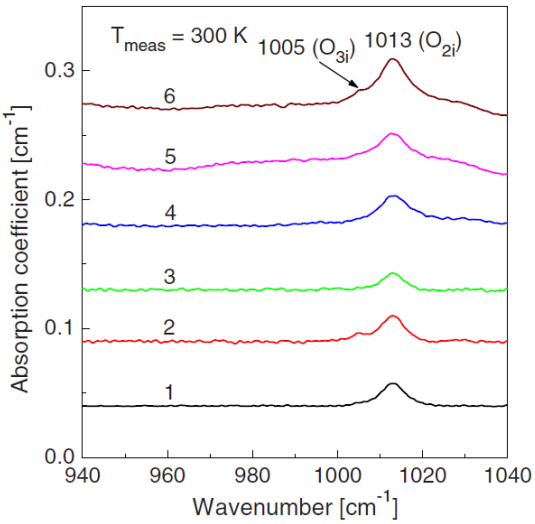

Figure 3.3: Infrared absorption spectra measured at 300 K with the resolution of 1 cm^{-1} for as-grown Cz-Si crystals with the following values of doping impurities and interstitial oxygen concentrations: 1-[B] = $1.5 \times 10^{14} cm^{-3}$, [$O_i$] = $1.2 \times 10^{18} cm^{-3}$; 2-[B] = $7 \times 10^{15} cm^{-3}$, [O_i] = $1.05 \times 10^{18} cm^{-3}$; 3-[B] = $8 \times 10^{14} cm^{-3}$, [O_i] = $9.5 \times 10^{17} cm^{-3}$; 4-[P] = $2 \times 10^{1}4 cm^{-3}$, [O_i] = $1.1 \times 10^{18} cm^{-3}$; 5-[P] = $7 \times 10^{14} cm^{-3}$, [O_i] = $1.0 \times 10^{18} cm^{-3}$; 6-[P] = $7 \times 10^{13} cm^{-3}$, [O_i] = $1.3 \times 10^{18} cm^{-3}$. The spectra are shifted on the vertical axis for clarity.

3.3.2 Local Vibrational Modes

We obtained two pairs of O-related LVMs for the O_{2i}^{st0} configuration of the dimmer, which is consistent with previous calculations. In order to compare with the infrared spectra we computed the relative intensities of the highest frequency pair, with modes located at 992 cm^{-1} and 954 cm^{-1} with relative intensities of 0.66 and 1.0 respectively. This splitting between the two modes is due to both vibrational coupling and a small difference between the two Si-O-Si units. By comparing our results with the experimentally observed LVMs frequencies we can see that they underestimate the experimental data by approximately 60 cm^{-1} for both modes. However, this is consistent with the 55 cm^{-1} underestimation made for the asymmetric mode of O_i. Our calculations also predict two pairs of LVMs for the O_{2i}^{sq++} configuration. The modes of the high frequency pair are located at 787-cm^{-1} and 702-cm^{-1} with relative intensity 0.00 and 2.16, respectively. In this case, since the defect is centro-symmetric, that is, both O atoms are equivalent, the splitting is only due to the vibrational coupling, where the split 787 cm^{-1} and 702 cm^{-1} modes correspond to symmetric and asymmetric stretching motions with respect to the inversion symmetry center. It shall be noted that, although the 787 cm^{-1} is IR inactive (0.00 relative intensity), the 702 cm^{-1} mode is predicted to be at least twice more intensive than than both high frenquency O_{2i}^{st0} related modes, and shall be easily observed. Therefore, this LVM in particular can work as an optical signature for the identification of O_{2i}^{sq++}.

3.3.3 Infrared spectra

We investigated the IR spectra of as-grown Cz-Si crystal samples, in order to search for the signature of O_{2i}^{sq++} related LVMs. Figure 3.3 shows the IR absorption spectra at 300 K. At this temperature, analysis based on resistivity measurements allows us to locate the equilibrium Fermi level in the ranges $E_c - (0.27 - 0.33)$ eV and $E_v + (0.22 - 0.32)$ eV for all n-type and p-type samples respectively. For the p-type samples, the condition of the Fermi level to be below $E_v + 0.47$ eV which has been predicted to be necessary for the oxygen dimmer to assume the O_{2i}^{sq++} configuration is fulfilled. The spectra presented in 3.3 shows us a dominant absorption line located at 1013 cm^{-1}, rising from O_{2i}^{st0} and assigned to the calculated 954-cm^{-1} band. Nevertheless, in the scrutinized frequency range, besides weak LVM lines related to substitutional boron defects, there are no additional lines in the spectra of p-type Si samples compared to those for n-type Si samples. We found no LVM lines at all in the frequency range of 650-800 cm^{-1}, which is a region where we expect to find evidence for the existence of O_{2i}^{sq++} related modes.
Figure 3.4 shows another set of IR spectra, measured at 15 K. At this temperature the equilibrium Fermi level position for n-type and p-type Cz-Si samples is estimated to be at $E_c - 0.05$ eV and $E_v + 0.05$ eV respectively. The two O_{2i}^{st0} related LVM lines located at 1012 cm^{-1} and 1060 cm^{-1} kept the same relative intensities in both Si sample types. Once again, no lines that can be related to the double positive squared configuration of the dimmer were detected. Figure 3.5 shows the dependencies of the intensity of the O_{2i}^{st0} related infrared absorption line with the concentration of interstitial oxygen, for the temperatures of 15 K (line at 1012 cm^{-1}) and 300 K (line at 1013 cm^{-1}), for samples with low carbon content. The data was fitted to a curve of the type $I_{O_{2i}^{st}} = A \times [O_i]^n$ with A and n as fitting parameters. We obtained $n = 1.82 \pm 0.25$ and $n = 1.94 \pm 0.13$ for the temperatures of 15 K and 300 K respectively. The fits are represented by the solid red lines in Fig. 3.5. The dependency of the intensity of the 1012 (1013) cm^{-1} bands with $[O_i]^2$ supports its assignment to the O_{2i} defect.

3.4 Conclusions

The obtained data shows no evidence supporting the existence of the double positively charged form of the dimmer in the temperature range 15-300 K, in all the n-type and p-type Si samples. On the other hand, the presence of the O_{2i}^{st0} is clearly evidenced in all the obtained infrared spectra measurements. In the absence of O_{2i}^{sq++}, the charge-driven migration mechanism for the oxygen dimmer is ruled out, and its diffusion at room temperatures is unlikely to occur. This result calls into question the well accepted B_sO_{2i} model for the photo-induced efficiency degradation of boron doped Cz-Si solar cells.

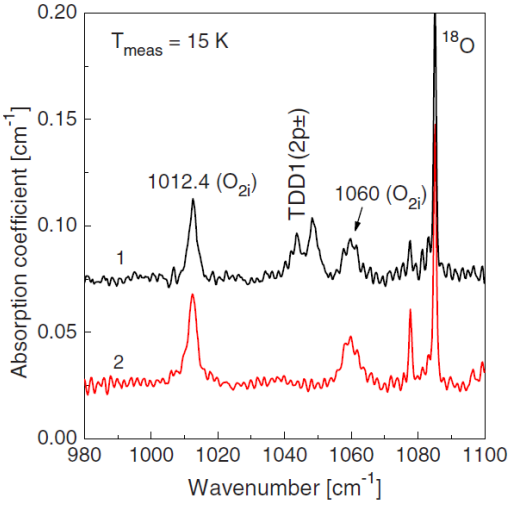

Figure 3.4: Infrared absorption spectra measured at 15 K with the resolution of 0.5 cm^{-1} for as-grown Cz-Si crystals with the following values of doping impurities and interstitial oxygen concentrations: 1-[B] = $1.5 \times 10^{15} cm^{-3}$,[$O_i$] = $9.5 \times 10^{17} cm^{-3}$; 2-[P] = $2 \times 10^{14} cm^{-3}$, [O_i] = $1.1 \times 10^{18} cm^{-3}$. The spectra are shifted on the vertical axis for clarity.

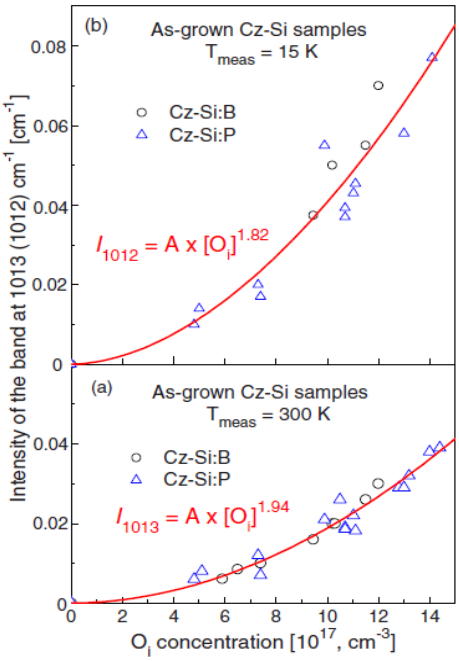

Figure 3.5: Intensity of IR absorption band at 1013 (1012) cm^{-1} due to staggered oxygen dimer measured at (a) 300 K and (b) 15 K vs interstitial oxygen concentration in as-grown Cz-Si samples.

Chapter 4

The B_iO_{2i} model for the light-induced degradation in B-doped Cz-Si solar cells

This chapter is based on the work published in A. Carvalho, P. Santos, J. Coutinho, R. Jones, M. J. Rayson, P. R. Briddon, *Physica Status Solidi*, **209**,1894 (2012)

4.1 Introduction

The results presented in the previous chapter raise questions concerning the validity of the B_sO_{2i} model, as being responsible for the light-induced degradation phenomena in silicon solar cells. The lack of evidence supporting the formation of O_{2i}^{++} complexes in silicon rules out the charge-driven migration mechanism, which hinders the possibility of the formation of defects such as the B_sO_{2i}. In addition, this model also fails to explain why, in B-P co-doped samples, the degradation depends on the hole density (p) rather than on the boron concentration [B] (Macdonald *et al*, 2009).
More recently, Voronkov and Falster (2010) proposed an alternative model, that assumes the existence of a latent complex consisting of a boron interstitial and an oxygen dimer (B_iO_{2i}). When the sample is exposed to the light, these latent complexes would suffer photon induced transformations and become active, in a time rate that is consistent with the slow degradation process. The formation of such complexes is justified with the dislocation of substitutional boron atoms to interstitial positions during the process of nucleation of oxygen precipitates in silicon that occurs in the course of crystal cooling. The newly formed B_i species would be able to disseminate in the crystal and find traps such as the oxygen dimmer, resulting in the formation of B_iO_{2i} complexes. Since B_i is a single-positive defect in p-type silicon, its solubility becomes proportional to hole concentration (p). On the other hand, this model is also compatible with the existing relation between the degradation center and the $[O_i]^2$, because it requires the presence of oxygen dimmer complexes able to trap the B_i species. In this chapter we investigate the stability and relative concentration of the B_i^+ and B_s^+ species. We also search for stable structures of the B_iO_{2i} defect and check their electrical activity. Finally we fit our results into the Voronkov and Falster degradation model in order to check for its consistency.

4.2 Method

The calculation conditions are similar to those presented in Section 2.2. However the energy cut off used for the plane-wave basis was 200 Ry. For O and B we used a total of 40 and 22 Gaussian basis functions, respectively. To obtain the results presented in the Subsection 4.3.1 we applied Si_{512} supercells, while in the Subsection 4.3.2, Si_{216} supercells were used. Unless otherwise specified, the electronic structure calculations presented in this chapter employed the marker method with crystaline silicon E_c and E_v levels used as markers. Calculations involving the nudged elastic band (NEB) method were performed with a set of 5 images.

4.3 Results

4.3.1 Formation energies and relative concentrations of boron related defects

In this section we present results concerning the relative formation energies and concentrations of the B_i (intrestitial boron) and B_s (substitutional boron) defects. The difference between the formation energies of these two defects in the neutral charge state is given by:

$$E_f[B_i] - E_f[B_s] = E[B_i] - E[B_s], \tag{4.1}$$

where $E[B_i]$ and $E[B_s]$ are the total energies of the defective supercells that host the B_i and B_s defects respectively. We obtained $E_f[B_i] - E_f[B_s] = 2.5$ eV.
Then we proceeded to the determination of the relative formation energies for different charge states. With that aim we calculated the electrical levels of both defects with the aid of the marker method. It is well established that the B_s defect is a shallow acceptor producing a $(-/0)$ level at $E_v + 0.045$ eV. To estimate this level we have used the valence band (the bulk $(0/+)$level) as a marker. On the other hand, the interstitial boron is a donor, producing a $(0/+)$ level at $E_c - 0.13$ eV. In this case we have chosen the substituional sulphur (S), a deep donor, as a marker. We obtained $B_s(-/0) = E_v + 0.00$ eV and $B_i(0/+) = E_c - 0.10$ eV, in good agreement with the aforementioned experimental values. Given the locations of these electrical levels in the gap, we can assume that, for a Fermi level in the region of the mid-gap $\mu_e \approx E_g/2$, the B_i defects are positively charged, whereas the B_s defects are negatively charged. Applying analogous expressions to the ones proposed in Eqs. 2.2 and 2.3 we obtained a 2.7 eV difference between the formation energies of both defects, when the Fermi level is located at mid-gap.
In thermal equilibrium, and at temperature T, the condition that minimizes the Gibbs free energy of the system gives us a relation between formation energy of a defect $E_f[X]$ and its concentration $[X]$:

$$[X] = [A_s] \exp(E_f[X]/kT), \tag{4.2}$$

where $[A_s] >> X$ is the concentration of available sites and k is the Boltzmann constant. Thus, for $\mu_e = E_g/2$, the ratio between $[B_i]$ and $[B_s]$ becomes:

$$\frac{[B_i]}{[B_s]} = \exp([E_f[B_i^+] - E_f[B_s^-]]/kT). \tag{4.3}$$

Considering a representative concentration of boron [B] = 10^{16} cm^{-3} we obtain [B_i] = 10^{-10} cm^{-3} at T=250 °C.

4.3.2 The B_iO_{2i} defect

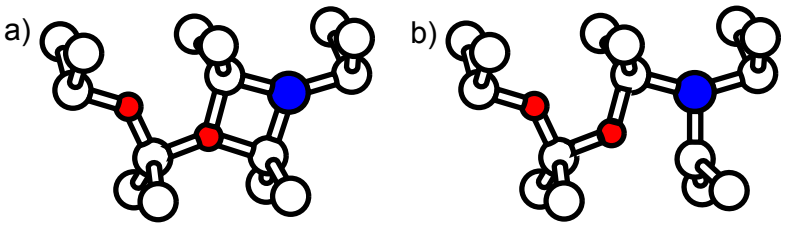

Figure 4.1: Atomic structure representation of the Ring form (a) and Open form (b) of the B_iO_{2i} defect

We calculated the total energies for 16 possible structures of the B_iO_{2i} defect, in different charge states. We found two particularly stable configurations which we labeled as *ring form* (R) and *open form* (O). These two configurations are depicted in Figs 4.1-a) and 4.1-b) respectively. The difference between the formation energies of these two configurations is $E_f[O^0] - E_f[R^0] = 0.1$ eV. We also employed the NEB method to analyse the reaction path that leads the transformation from the R^0 configuration to a less stable O^0 configuration. The saddle point of this reaction corresponds to the breaking of a Si-O bond, which has an associated energy barrier of 0.31 eV. This value is explained by the fact that the oxygen atom leaves a high-energy over-coordinated configuration to a more stable two-fold coordinated structure, lowering the total energetic cost associated to the Si-O bound breaking.
In Figure 4.1 we can observe, in both configurations, features that indicate the existence of electrical activity: While the R-form has an over-coordinated oxygen atom (bonds with 3 Si atoms), the O-form has an under coordinated Si atom. We investigated the electrical activity of both configurations and found a shallow (0/+) level related to the R-form at $E_v + 1.02$ eV and a deep donor at $E_v + 0.48$ eV, related to the O-form. We also report an energy difference between both configurations in the positively charged state of $E_f[O^+] - E_f[R^+] = 0.1$ eV. At this charge state, the open form is metastable, and spontaneously relaxes to the more stable R^+ configuration.
These results are not consistent with the expected behaviour of the minority carrier trap capable of inducing the degradation. The shallow donor level produced by the most stable structure (R-form) does not match the predicted $E_v + 0.35$ to $E_c - 0.45$ region for the minority carrier trap. On the other hand, Although the O-form is able to produce a deep donor level closer to that region, its high formation energy relatively to the R-form makes it marginally stable at room temperature in p-type Si (even in the dark). In Figure 4.2 we present a Energy-Configuration diagram that summarizes our results and puts them in the perspective of the Voronkov and Falster degradation model. The several reconfiguration steps are described in detail in the figure caption.

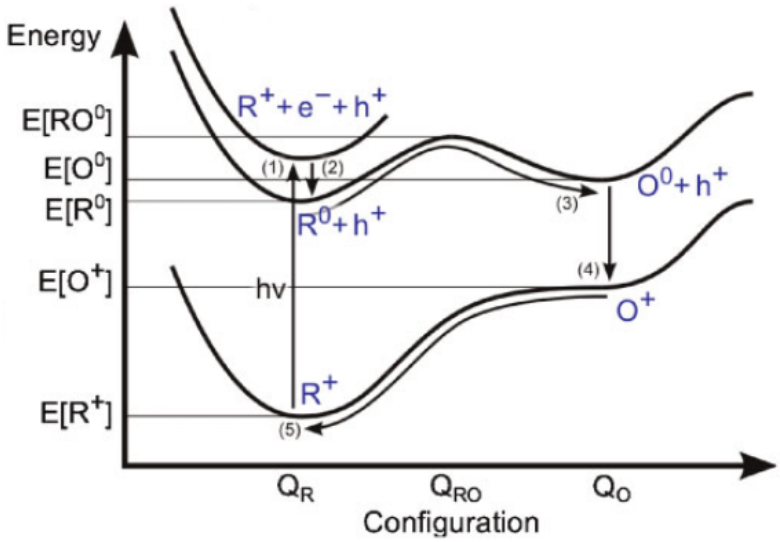

Figure 4.2: Configuration diagram of the B_iO_{2i} defect. (1) absorption of a photon with energy $h\nu$, promoting the formation of a hole-electron pair in the material. (2), The positively charged Ring form captures the newly promoted electron.(3) migration from R^0 to O^0 with an energy barrier of 0.31 eV. (4) The neutral open form of the B_iO2_i captures the hole, becoming metastable and spontaneously reconfigures into the positively charged ring form(5).

4.4 Conclusions

Given the results presented in the last two chapters, neither the B_sO_{2i} defect nor the B_iO_{2i} are suitable representatives of the slow forming recombination center that causes the severe degradation step of the Cz-Si solar cells.
Firstly, we found out that the presence of interstitial boron atoms in B-doped Cz-Si was estimated to be almost negligible, and can hardly be related to the degradation problem. Finaly we investigated the electrical activity of the B_iO_{2i}. We found the existence of a shallow donor produced by the most stable form of the defect (R-form) that cannot be related to the SRC electrical activity. We also found a O-form related deep donor level, closer to the region of the SRC trap level. However, given the existing migration barrier of ≈ 0.3 eV associated to the R $\rightarrow$ O path, and the higher formation energy of the O-form of the defect, its formation should not occur at room temperature.

Bibliography

J. Adey, R. Jones, D. W. Palmer, P. R. Briddon, and S. Öberg, *Physical Review Letters* **93**, 055504 (2004).

M. Ahmed, S. J. Watts, J. Matheson, and A. Holmes-Siedleb, *Nuclear Instruments and Methods in Physics Research A*, **457**, 588 (2001).

U. von Barth and L. Hedin , *Journal of Physics C* **5**, 1629 (1972).

M. Born and K. Huang, *Dynamical Theory of Crystal Lattices* (Oxford University Press, Oxford, 1954).

M. Born and R. Oppenheimer, *Annalen der Physik* **87**, 457 (1925).

J. C. Bourgoin and J.W. Corbett, *Physics Letters A* **38**, 135 (1972).

K. Bothe and J. Schmidt, *Journal of Applied Physics* **99**, 013701 (2006).

K. Bothe, J. Schmidt, and R. Hezel, in *Proceedings of the 3rd World Conference on Photovoltaic Energy Conversion*(Osaka, Japan 2003), p.2887

Brust D, in *Methods in Computational Physics* volume 8, p. 33 (Academic Press, 1968).

D.M. Ceperley, *Physical Review B* **18**, 3126 (1978).

D.M. Ceperleyand and B.J. Alder, Physical Review Letters **45**, 566 (1980).

D. J. Chadi and K. J. Chang, *Physical Review B* **38**, 1523 (1988).

John W. Cleland, *Journal of the Electrochemical Society* **129**, 2127 (1982)

J. Coutinho, V. J. B. Torres, R. Jones, and P. R. Briddon, *Physical Review B* **67**, 035205 (2003).

A. Dierlamm, *Nuclear Instruments and Methods in Physics Research A*, **624**, 396 (2010).

S.T. Epstein, A.C Hurley, R.E. Wyatt, and R.G. Parr, Journal of Chemical Physiscs **47**, 1275 (1967).

S.W. Glunz, S. Rein, W. Warta, J. Knobloch, and W. Wettling, in *Proceedings of the 2nd World Conference on Photovoltaic Energy Conversion* (European Commission, Ispra, Italy, 1998), p. 1343.

Harrison W A, *Pseudopotentials in the theory of metals (W. A. Benjamim, New york* (1966).

C. Hartwigsen, S. Goedecker, and J. Hutter, *Physical Review B* **58**, 3641-3662 (1998).

J. L. Hastings, S. K. Estreicher, and P. A. Fedders, *Physical Review B* **56**, 10215 (1997)

Heine V, *Solid State Physics 24*, **1** (1970).

G. Henkelman, B.P. Uberuaga, and H. Jnsson, *Journal Chemical Physics*, **113**, 9901 (2000).

P. Hohenberg and W. Kohn, *Physica Review* **136**, 864 (1964).

B. Hourahine, R. Jones, A.N. Safonov, S. O berg, P. R. Briddon, and S. K. Estreicher, *Physical Review B* **61**, 12594-12597 (2000).

W. Kohn and L. J. Sham, *Physical Review* **140**, A1133 (1965).

Y.-H. Lee and J. W. Corbett, *Physical Review B*, **9**, 4351 (1974).

D. Macdonald, F. Rougieux, A. Cuevas, B. Lim, J. Schmidt, M. Di Sabatino, and L. J. Geerligs, *Journal of Applied Physics 105*, 093704 (2009).

D.V. Makhov and L. J. Lewis, *Physical Review Letters* **92**, 255504 (2004).

V. P. Markevich, A. R. Peaker, S. B. Lastovskii, L. I. Murin, J. Coutinho, V. J. B. Torres, P. R. Briddon, L. Dobaczewski, E.V. Monakhov, and B. G. Svensson, *Physical Review B* **80**, 235207 (2009).

P. J. Mohr and B. N. Taylor, *Review of Modern Physics*, **72**, 351 (2000).

M. Moll, E. Fretwurst, M. Kuhnke, and G. Lindstrm, *Nuclear Instruments and Methods in Physics Research B* **186**, 100 (2002).

H.J. Monkhorst and J.D. Pack, *Physical Review B* **13**, 5188 (1976).

J.D. Pack and H.J. Monkhorst, *Physical Review B* **16**, 1748 (1977).

R. G. Parr and W. Yang, *Density-Functional Theory of Atoms and Molecules* (Oxford University Press, New York, 1989).

J. P. Perdew , in *Electronic Structure of Solids* '91, (edited by P Ziesche and H Eschrig) (Akademie Verlag, Berlin, 1991).

J. P. Perdew and Y. Wang , *Physical Review B***45**, 13244 (1992).

J. P. Perdew and A. Zunger, *Physical Review B* **23**, 5048 (1981).

Pickett W E, *Computational Physics Reports* **9**, 115 (1989).

J. A. Pople and D.L. Beverage, *Approximate Molecular Orbital Theory* (McGraw-Hill, New-York, 1970).

S. Rein, T. Rehrl,W.Warta, S.W. Glunz, and G.Willeke, in *Proceedings of the 17th European Photovoltaic Solar Energy Conference* (WIP-ETA, Munich, 2001), p. 1555.

S. Rein and S.W. Glunz, *Applied Physics Letters* **82**, 1054 (2003).

J. Schmidt and A. Cuevas, *Journal of Applied Physics* **86**, 3175(1999).

J. Schmidt, K. Bothe, and R. Hezel, in *Proceedings of the 29th IEEE Photovoltaic Specialists Conference*(IEEE, New York, 2002), p. 178.

Stoneham A M, *Theory of Defects in Solids* (Oxford University Press, London, 1975).

B. G. Svensson, B. Mohadjeri, A. Halln, J. H. Svensson, and J. W. Corbett, *Physical Review B*, **43**, 2292 (1991).

T. Taishi, T. Hoshikawa, M. Yamatani, K. Shirasawa, X. Huang, S. Uda, K. Hoshikawa, *Journal of Crystal Growth* **306**, 452(2007)

M. Trauwaert, J. Vanhellemont, H. E. Maes, A. V. Bavel, G. Langouche, and P. Clauws, *Applied Physics Letters* **66**, 3056 (1995).

V. V. Voronkov and R. Falster, *Journal of Applied Physics* **107**, 053509 (2010).

Vosko S. H., Wilk L., and Nusair M., *Canadian Journal of Physics* **58**, 1200 (1980).

G. D. Watkins and J. W. Corbett, *Physical Review* **138**, A543 (1965).

G. D. Watkins, "Deep centers in semiconductors," (Gordon and Breach Science Publishers, New York, 1992) Chapter 3, page 177, 2^{nd} edition.

J. Zhao, A. Wang, M. A. Green, and F. Ferrazza, *Applied Physics Letters*, **73**, 1991 (1998).